Understanding Complete Oxidation of Methane on Spinel Oxides at Molecular Level

Understanding complete oxidation of methane on spinel oxides at a molecular level

Franklin Feng Tao[1,2], Jun-jun Shan[1,2,*], Luan Nguyen[1,2,*], Ziyun Wang[3,*], Shiran Zhang[1,2], Li Zhang[4], Zili Wu[4], Weixin Huang[1,2], Shibi Zeng[1,2] & P. Hu[3]

1. Department of Chemical and Petroleum Engineering, University of Kansas, Lawrence, Kansas 66045, USA. 2. Department of Chemistry, University of Kansas, Lawrence, Kansas 66045, USA.

3. School of Chemistry and Chemical Engineering, Queens University, Belfast BT9 5AG, UK. 4. Center for Nanophase Materials Sciences and Chemical Science Division, Oak Ridge National Laboratory Oak Ridge, Tennessee 37831, USA. * These authors contributed equally to this work. Correspondence and requests for materials should be addressed to F.F.T. (email: franklin.feng.tao@ku.edu) or to P.H. (email: p.hu@qub.ac.uk).

It is crucial to develop a catalyst made of earth-abundant elements highly active for a complete oxidation of methane at a relatively low temperature. $NiCo_2O_4$ consisting of earth-abundant elements which can completely oxidize methane in the temperature range of 350–550°C. Being a cost-effective catalyst, $NiCo_2O_4$ exhibits activity higher than precious-metal-based catalysts. Here we report that the higher catalytic activity at the relatively low temperature results from the integration of nickel cations, cobalt cations and surface lattice oxygen atoms/oxygen vacancies at the atomic scale. In situ studies of complete oxidation of methane on $NiCo_2O_4$ and theoretical simulations show that methane dissociates to methyl on nickel cations and then couple with surface lattice oxygen atoms to form $-CH_3O$ with a following dehydrogenation to CH_2O; a following oxidative dehydrogenation forms CHO; CHO is transformed to product molecules through two different sub-pathways including dehydrogenation of OCHO and CO oxidation.

A complete oxidation of hydrocarbons has been a significant topic in the field of heterogeneous catalysis for decades since unburned hydrocarbons must be transformed in power plants or before release of gas exhaust from various engines of vehicles using gasoline, diesel, natural gas or liquid petroleum gas (a mixture of propane, isobutene, *n*-butane and ethane). Thermal stability of a catalyst (for removal of CH_4 or other hydrocarbons) at a temperature of 1,300 °C for applications to power plants or at least 800 °C for engines using gasoline or diesel is requested. Ying *et al.* reported that CeO_2 nanoparticles supported on barium hexaaluminate exhibits high activity at a quite high temperature and remains its structure up to 1,300 °C (ref. 1). Recently, Gorte, Fornasiero, and Farrauto and their coworkers reported that a catalyst of Pd nanoparticles caged in a porous CeO_2 shell supported on Al_2O_3 exhibits exceptionally high activity for a complete oxidation of methane with a high thermal stability up to 850 °C (refs 2,3). The activity of $Co_{3-x}Cu_xO_4$, $Co_{3-x}Zn_xO_4$, and $Co_{3-x}Ni_xO_4$ for oxidation of hydrocarbons was reported in 1968 and the following studies[4–7]. A very recent study showed the high activity of these oxides in oxidation of (a) a mixture of liquefied petroleum gas and CO or (b) a liquefied petroleum gas without CO[8].

Use of natural gas vehicles is a programme launched in Europe and other countries towards diversity of energy sources and utilization of methane, the inexpensive, earth-abundant energy sources[9–12]. The exhaust of natural gas engines has the following features[9]: low temperature (<500–550 °C), low CH_4 concentration (about 1,000 p.p.m.), large amount of water vapour (10%), high O_2:CH_4 ratio, and presence of NO_x or SO_x (refs 9,12). A complete oxidation of methane at a relatively low temperature (<500–550 °C) is critical for abating unburned methane of the exhaust of engines of natural gas vehicles[9,11–13]. Pt and Pd supported on Al_2O_3 are the well-studied catalysts[9]. Significant efforts have been made in fundamental understanding of mechanism of the complete oxidation of methane[14] and optimization of catalytic performances of these Pt- or Pd-based catalysts[9]. From reaction mechanism point of view, Neurock and Iglesia *et al.* first elucidated the reaction mechanism on Pd-based catalysts at a molecular level[14]; these Pd-based catalysts exhibit different mechanisms of activation of C–H along increase of chemical potential of oxygen.

The high cost of precious metals has driven the search of catalysts made of earth-abundant elements. Spinel oxide, a type of reducible early transition metal oxides, consists of M^{2+} and M^{3+} in its lattice. Co_3O_4 is one of the spinel oxides. It has almost weakest M–O bonds among all transition metal oxides[15,16]. Oxygen vacancies can be readily generated even at a temperature below 25 °C (refs 17,18). In addition, the barrier for hopping oxygen vacancies on the surface of Co_3O_4 is only 0.23 eV (ref. 17). Due to the high density of oxygen vacancies of surface of Co_3O_4 (refs 15,19), Ni cations and oxygen vacancies are mixed at atomic scale, while Ni cations are integrated to the lattice of Co_3O_4 through formation of a doped spinel oxide $Ni_xCo_{3-x}O_4$. Figure 1a schematically shows the integration of Ni cations, Co cations and surface lattice oxygen atoms and vacancies at atomic scale. Although catalytic activity of a complete oxidation of hydrocarbons on doped cobalt oxides was reported as early as 1968 (refs 4–8), there is lack of mechanistic understanding of the complete oxidation of hydrocarbons at a molecular level. Compared with the well-studied complete oxidation of CH_4 on Pt or Pd-based catalysts[9], the complete oxidation on $NiCo_2O_4$ could fellow a different mechanism.

Here we focus on mechanistic exploration of a complete oxidation of methane on $NiCo_2O_4$ at a molecular level. Multiple *in situ* techniques are used in experimental exploration of the catalytic mechanism. Surface chemistry of this mixed oxide during catalysis is tracked with ambient pressure X-ray photoelectron spectroscopy (AP-XPS)[20]. Vibrational signature of surface adsorbates is identified with *in situ* infrared spectroscopy. In addition, computational studies for understanding of the mechanism of the complete oxidation of methane on $NiCo_2O_4$ at a molecular scale are performed.

Results

Catalytic performance for complete oxidation of CH_4. Catalyst $NiCo_2O_4$ was synthesized with a coprecipitation method described in the section of Methods. X-ray diffraction (Fig. 1b) showed that $NiCo_2O_4$ nanoparticles have the same spinel structure as Co_3O_4. $NiCo_2O_4$ catalyst consists of nanoparticles with a size of 3–6 nm (transmission electron microscopic (TEM) images; Fig. 1c,d). With the same method, $Ni_{0.75}Co_{2.25}O_4$ and $Ni_{1.25}Co_{1.75}O_4$ were prepared. X-ray diffraction and TEM studies confirmed the formation of lattice of spinel oxide (Supplementary Figures 1 and 2, and Supplementary Methods).

Catalytic performances of a complete oxidation of CH_4 on these catalysts were measured in a fixed-bed flow reactor. Certain amount of a catalyst given in figure captions was used in different experiments. 10% CH_4 balanced with Ar, and 99.99% O_2, and 99.99% Ar with certain flow rates were mixed and then flowed through a catalyst bed. The molar ratio of the introduced CH_4 and O_2 is 1:5 for all experiments in Fig. 2. $NiCo_2O_4$ is extraordinarily active in combustion of CH_4 to CO_2 and H_2O. CH_4 is completely combusted at 350 °C, while gas hourly space velocity (GHSV) of methane is 24,000 ml 5% $CH_4\,g^{-1}\,h^{-1}$ (Fig. 2). At the same GHSV, pure Co_3O_4 and pure commercial

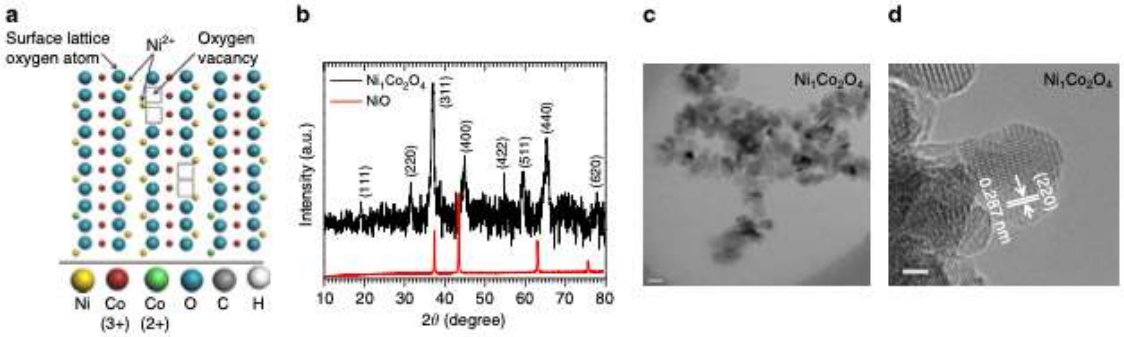

Figure 1 | $NiCo_2O_4$ catalyst for a complete oxidation of methane. (**a**) Schematic showing a surface of $NiCo_2O_4$ catalyst. (**b**) XRD pattern of $NiCo_2O_4$ catalyst. (**c**) Large-scale TEM image; scale bar, 10 nm. (**d**) High-resolution TEM image; scale bar, 2 nm.

NiO with surface areas similar to $NiCo_2O_4$ exhibit a conversion of only 8% and 0% at 350 °C, respectively (Fig. 2). The pure Co_3O_4 without any Ni cations exhibits a much lower conversion than $NiCo_2O_4$ though it has the same lattice of a spinel structure. This distinct difference in catalytic performance between $NiCo_2O_4$ and pure Co_3O_4 in the temperature range of 200–425 °C shows that Ni cations are crucial sites for dissociation of CH_4, which was supported by experimental studies and theoretical findings in the following sections. The catalytic performance of complete combustion at 350 °C is remained even after heating to 550 °C and then cooling to 200 °C (Fig. 3a). Kinetic studies were performed in the temperature range of 270–330 °C, while catalysis was in a kinetics control regime by controlling conversions $<10\%$. The measured activation barrier is about 108 kJ mol^{-1} (Supplementary Fig. 3). In addition, $NiCo_2O_4$ exhibits durability in complete oxidation of methane at 350 °C and 550 °C for over 48 h (Fig. 3b,c). The thermal stability of catalyst structure was confirmed by the preservation of X-ray diffraction pattern of $NiCo_2O_4$ after a complete oxidation at 550 °C (Supplementary Fig. 4). In addition, $NiCo_2O_4$ remains the original particle size after a complete oxidation at 550 °C as shown in Supplementary Fig. 5. This is consistent with the thermal stability of $NiCo_2O_4$ suggested by the thermal analysis of coprecipitated products and $NiCo_2O_4$ (ref. 21).

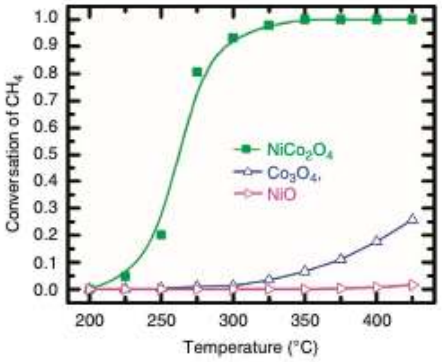

Figure 2 | Conversion of CH_4. Conversion of CH_4 in a complete oxidation of CH_4 on $NiCo_2O_4$ in the temperature range of 200–425 °C . The gas composition of the feed gas is 5% CH_4, 25% O_2 and 70% Ar. Molar ratio of CH_4 to O_2 in the gas mixture is always 1:5. As 500 mg $NiCo_2O_4$ catalyst was used, the GHSV of CH_4 is 24,000 ml 5% CH_4 g^{-1} h^{-1}; at this GHSV the conversion of CH_4 on $NiCo_2O_4$ at 350 °C is 100%.

Surface chemistry of $NiCo_2O_4$ during catalysis. Measurements of bulk composition of $NiCo_2O_4$ catalyst using inductively coupled plasma Auger electron spectroscopy show that atomic ratio of Ni and Co in bulk of the $NiCo_2O_4$ nanoparticles is 1:2. Similar to the obvious difference in composition of bimetallic nanoparticle between surface and bulk[22], the difference in atomic ratio of Ni/Co of $NiCo_2O_4$ catalyst between surface and bulk was uncovered here as well.

To achieve a deep understanding of the complete oxidation of methane on $NiCo_2O_4$, we performed *in situ* studies using AP-XPS[15,20,23,24] in the temperature range of 60–400 °C by following the reaction conditions used for measurements of catalytic performances in a fixed-bed flow reactor. Surface chemistry of $NiCo_2O_4$ (a) in UHV, (b) in a reactant gas (CH_4 or O_2) at room temperature, (c) in a mixture of reactant gases ($CH_4 + O_2$) at room temperature and (d) in a mixture of reactant gases ($CH_4 + O_2$) in the temperature range of 25–400 °C were studied. Photoemission features of Co 2*p*, Ni 2*p*, and O 1*s* of $NiCo_2O_4$ collected under conditions (a), (b) and (c) are quite similar; in addition, the atomic ratios of O/(Ni + Co) of the catalyst surface under the three conditions are the same. However, the atomic ratio O/(Ni + Co) in the gaseous environment of CH_4 and O_2 exhibits a temperature-dependent evolution which will be discussed in the following paragraphs.

During the data acquisition of *in situ* studies, $NiCo_2O_4$ catalyst was remained in a mixture of CH_4 and O_2 (molar ratio 1:5) in Torr pressure range. Figure 4, Supplementary Fig. 6 and Supplementary Fig. 7 present photoemission features of $NiCo_2O_4$, $Ni_{0.75}Co_{2.25}O_4$ and $Ni_{1.25}Co_{1.75}O_4$ during catalysis, respectively. As shown in Fig. 4a,b, the photoemission features of Ni 2*p* and Co 2*p* remain constant in the temperature ranges of 60–400 °C. Surprisingly, two C 1*s* peaks at 285.6 eV (peak 1) and 288.3 (peak 2) were clearly observed even at 60 °C (Fig. 4d). Figure 5a shows the evolution of the surface atomic ratio, $\frac{C}{Ni+Co}$ of the two C 1*s* peaks of Fig. 4d along the increase of catalysis temperature. One interesting evolution is a quick increase of species 2 (peak 2 in Fig. 4d), a following decrease, and then a nearly complete disappearance of this species at about 250 °C (red lines in Fig. 5a,b) where the conversion of CH_4 starts to increase largely (Fig. 2). The sharp decrease of $\frac{C_{peak2}}{Ni+Co}$ on $NiCo_2O_4$ (red line in Fig. 5a) and a following decrease and then disappearance at 250–300 °C along the rapid increase of catalytic

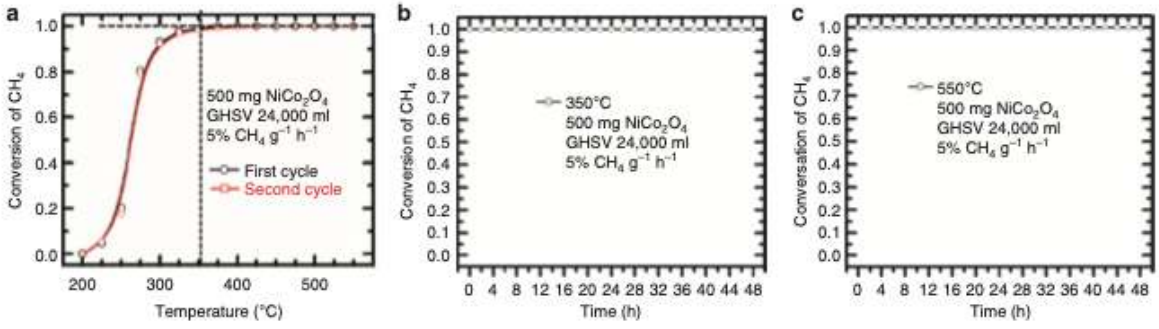

Figure 3 | Catalytic performances of $NiCo_2O_4$ in the temperature range of 200–550 °C. (**a**) CH_4 can be completely oxidized at a temperature up to 550 °C (black line), and the catalytic performance remains the same after heating to 550 °C and then cooling to 200 °C (red line). (**b**) Conversion of a complete oxidation of CH_4 on $NiCo_2O_4$ at 350 °C for 48 h. (**c**) Conversion of a complete oxidation of CH_4 on $NiCo_2O_4$ at 550 °C for 48 h.

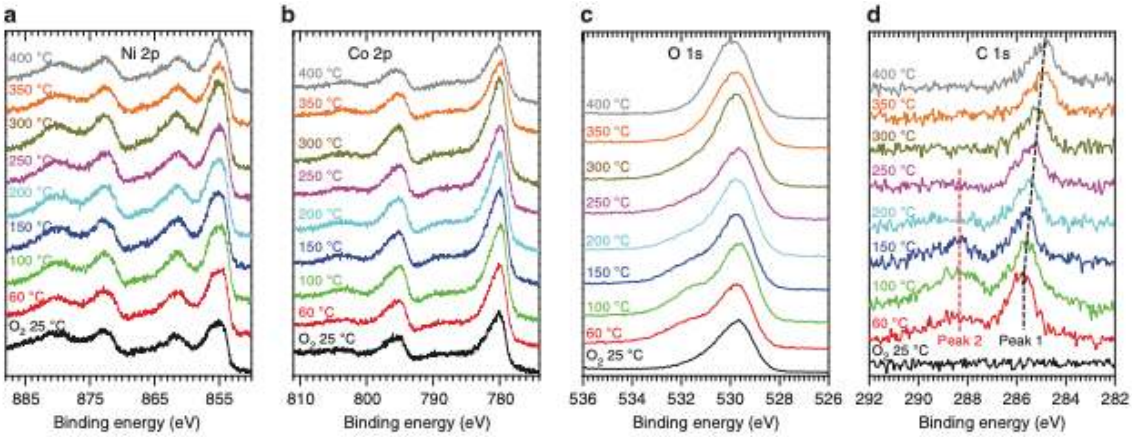

Figure 4 | Photoemission features. Photoemission features of $NiCo_2O_4$ at different temperatures during catalysis on $NiCo_2O_4$ in CH_4 and O_2 with a molar ratio of 1:5 at Torr pressure range. (**a**) Ni 2*p*, (**b**) Co 2*p*, (**c**) O 1*s*, and (**d**) C 1*s*.

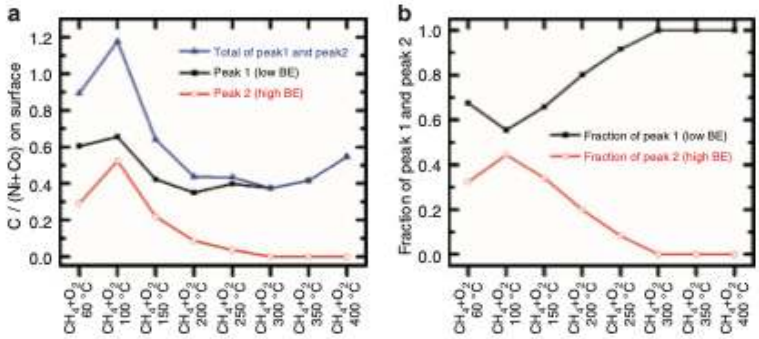

Figure 5 | Evolution of surface concentration of carbon-containing species. Evolution of surface concentration of carbon-containing species during catalysis at different temperature based on *in situ* studies of $NiCo_2O_4$ surface by AP-XPS. (**a**) Atomic ratio of $\frac{C_{total}}{Ni+Co}$, $\frac{C_{peak1}}{Ni+Co}$, and $\frac{C_{peak2}}{Ni+Co}$ and (**b**) atomic fraction of carbon species 1 (peak 1), $\frac{C_{peak1}}{C_{total}}$ and carbon species 2 (peak 2), $\frac{C_{peak2}}{C_{total}}$ at different temperatures. The error of measurement of peak area is ±5% of the corresponding peak area.

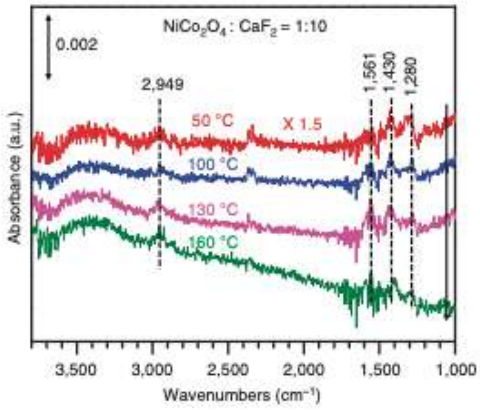

Figure 6 | *In situ* infrared studies. *In situ* infrared studies of the surface species on $NiCo_2O_4$ catalyst in the mixture with CaF_2 under the same catalytic condition as the measurement of catalytic performance in a fixed-bed flow reactor.

conversion at 250–300 °C (green line in Fig. 2) suggests species 2 (peak 2 in Fig. 4d) is an intermediate in the formation of CO_2 molecules.

In situ infrared studies of catalysts helped assign the two species corresponding to peaks 1 and 2 in Fig. 4d. As shown in Fig. 6, vibrational peaks at 1,280 1,430 and 1,561 cm^{-1} were observed in the temperature range of 50–160 °C. Referred to the literature[25], these vibrational signatures are contributed from formate species (OCHO). The assignment of these vibrational peaks to a formate species is supported by the agreement between C 1*s* photoemission peak at 288.3 eV (peak 2 in Fig. 4d) and 288.5 eV of the reported formate species[25]. Thus, both *in situ* photoemission feature of C 1*s* and *in situ* vibrational signature of surface species suggest the formation of OCHO species on the surface at a relatively low temperature. C–H vibrational peaks at 2,900–3,000 cm^{-1} were identified during *in situ* studies of CH_4 combustion on $NiCo_2O_4$. They are contributed from C–H stretching of the spectator CH_n species formed from dissociative adsorption of CH_4, supported by the low C 1*s* binding energy of CH_n (peak 1) at 285.9–284.8 eV (refs 25–27), and C–H stretching of the intermediate OCHO.

To investigate whether that the C 1*s* photoemission feature at 284.9–285.8 eV (peak 1 in Fig. 4d) is assigned to adsorbed CH_n species or accumulated atomic carbon of coke, surface of the active catalyst at 400 °C or 140–200 °C in the mixture of CH_4 and O_2 (1:5) was tracked on CH_4 was purged but O_2 kept. The *in situ* AP-XPS (Supplementary Fig. 8) suggests that the left CH_n species on surface at 400 °C reacted with oxygen upon CH_4 was purged

and but O_2 remained. As shown in Supplementary Fig. 8, C 1*s* photoemission feature of the left CH_n species disappeared within a few minutes due to a quick oxidation by O_2 to form CO_2. A similar study was designed to test whether the peak 1 of C 1*s* spectrum observed at 150 °C in the mixture of CH_4 and O_2 (1:5) (Fig. 4d) is coke-like carbon or chemisorbed CH_n species. As shown in Supplementary Fig. 9, these carbon-containing species formed at 140 °C reacted with O_2 to form CO_2 and disappeared at 200 °C in O_2. Therefore, these designed experiments (Supplementary Figs 8 and 9) suggest that the C1*s* at 284.9–285.8 eV (peak 1) is not contributed from accumulated coke-like carbon since a coke-like carbon is not readily oxidized to CO_2 at 400 °C or 140–200 °C (ref. 28). Therefore, both C 1*s* photoemission feature and C–H vibrational signatures allow us for assigning the carbon-containing species of peak 1 in Fig. 4d to CH_n species. It is noted that the coke-like carbon does form by dissociation of CH_4 when $NiCo_2O_4$ catalyst is kept in pure CH_4 (Supplementary Fig. 10d); in addition, without O_2, nickel cations of $NiCo_2O_4$ are reduced to metallic state at 400 °C (Supplementary Fig. 10a); along this reduction, coke-like carbon are formed at 400 °C (Supplementary Fig. 10d). It suggests a strong binding of coke-like carbon on metallic Ni atoms[28]. By introducing O_2 to the surface of carbon layers at 400 °C, the C 1*s* photoemission feature of coke-like carbon still remains. It further suggests the nature of coke-like carbon formed on $NiCo_2O_4$ in the lack of molecular O_2. By introducing the mixture of CH_4 and O_2 (1:5) to this surface covered with a layer of coke, there is no conversion of CH_4 anymore on it since the catalyst surface has been coved with coke-like carbon.

Figure 7a presents the evolution of the surface atomic ratio, $\frac{O}{Ni+Co}$ along the increase of catalysis temperature of $NiCo_2O_4$. There are two processes involved in the evolution of $\frac{O}{Ni+Co}$ atom ratio. The formation of OCHO species with a following desorption of CO_2 generates surface oxygen vacancies; an opposite process is the filling of oxygen vacancies with oxygen atoms through dissociation of molecular O_2. The 'U' shape evolution of $\frac{O}{Ni+Co}$ atomic ratio shows that more oxygen vacancies are created at a medium temperature (150–250 °C). The decrease of the ratio, $\frac{O}{Ni+Co}$ (namely, the increase of density of oxygen vacancies) at $\leq$250 °C likely suggests that the formation of oxygen vacancies through desorption of product molecules is relatively faster than filling oxygen vacancies through dissociation of O_2 in this temperature range. At a relatively high temperature such as 300 °C, the $\frac{O}{Ni+Co}$ atomic ratio starts to increase. It probably results from the accelerated dissociation of O_2 and thus a faster refilling of surface oxygen vacancies (at a higher temperature) than consumption of oxygen atoms through transforming the OCHO intermediate to product molecules CO_2. The turning point of $\frac{O}{Ni+Co}$ ratio (about 250 °C) suggests that there is a barrier for O_2 dissociation. For a temperature $\leq$250 °C, the filling of oxygen vacancies through dissociation of molecular O_2 on oxygen vacancies is kinetically slower than the creation of oxygen vacancies through desorption of intermediate or product molecules; thus, the net outcome is the decrease of $\frac{O}{Ni+Co}$ ratio at a relatively low temperature. At a relatively high temperature ($\geq$250 °C), however, dissociation of O_2 is accelerated and thus oxygen vacancies are filled rapidly; therefore, the overall consequence is the increase of surface lattice oxygen at a temperature $\geq$250 °C. Alternatively, a potential oxygen-containing spectator could possibly be formed. It may contribute to the increase of O/(Ni + Co) ratio. Very similar 'U-shape' evolution of $\frac{O}{Ni+Co}$ atomic ratio was observed on $Ni_{0.75}Co_{2.25}O_4$ and $Ni_{1.25}Co_{1.75}O_4$ (Fig. 7b,c) along the increase of the catalysis temperature of complete oxidation of methane.

***In situ* studies using isotope-labelled reactant and catalyst.** Both *in situ* AP-XPS and infrared studies have shown the formation of the two species on $NiCo_2O_4$ surface in the mixture of CH_4 and O_2, formate (species 2) and CH_n (n = 0–3; species 1). To elucidate the source of oxygen atoms of the intermediate of OCHO species, we performed two temperature programmed reactions using isotope-labelled reactant and isotope-labeled catalyst: (1) CH_4 and O_2^{18}on $NiCo_2O_4^{16}$ (Fig. 8a) and (2) CH_4 and O_2^{16}on an isotope-labeled catalyst ($NiCo_2O_{4-x}^{16}O_x^{18}$) (Fig. 8b).

In the complete oxidation of CH_4 in O_2^{18} on $NiCo_2O_4^{16}$ (Fig. 8a), products formed in the reaction cell of the AP-XPS were measured with an on-line mass spectrometer. One of the products, $CO^{16}O^{18}$ (M/z = 46; green line in Fig. 8a) was clearly observed. The formation of $CO^{16}O^{18}$ suggests that surface lattice oxygen atoms O^{16} of $NiCo_2O_4^{16}$ participated into the formation of CO_2 since the reactant gas O_2^{18} does not have O^{16} atoms. The co-existence of O^{16} and O^{18} in $CO^{16}O^{18}$ product suggests that molecular O_2 dissociates on surface during complete oxidation of CH_4.

Another experiment is the CH_4 combustion in O_2^{16}on an isotope-labeled catalyst $NiCo_2O_{4-x}^{16}O_x^{18}$ (Fig. 8b). The isotope-labeled catalyst $NiCo_2O_{4-x}^{16}O_x^{18}$ was prepared by annealing the catalyst $NiCo_2O_4^{16}$ to 350 °C in a flowing O_2^{18}. The preparation of $NiCo_2O_{4-x}^{16}O_x^{18}$ was done in an attached high-pressure reactor of AP-XPS system which is different from the reaction cell of AP-XPS since our AP-XPS system has both reaction cell for AP-XPS studies and high-pressure reactor for pretreatment.

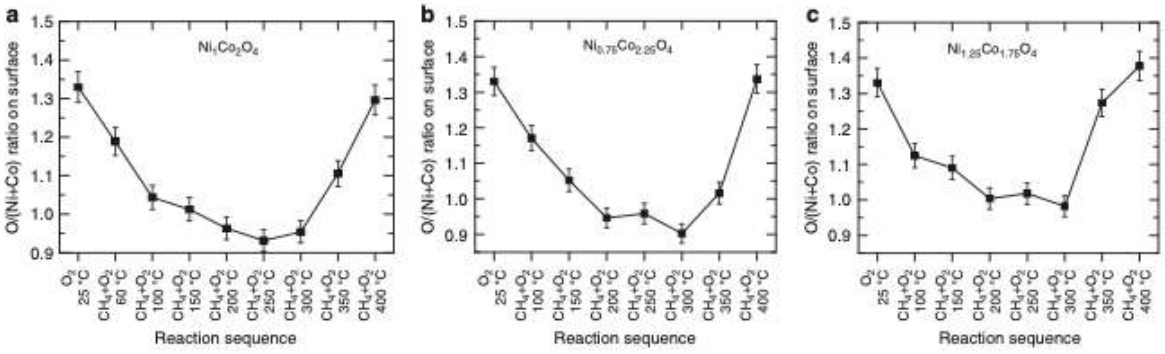

Figure 7 | Evolution of atomic ratio of oxygen atoms. Evolution of atomic ratio of oxygen atoms to the total of Ni and Co in surface region of three catalysts $NiCo_2O_4$ (**a**), $Ni_{0.75}Co_{2.25}O_4$ (**b**) and $Ni_{1.25}Co_{1.75}O_4$ (**c**) along the increase of catalytic temperature during catalysis. The error of measurement of peak area is ±5% of the corresponding peak area.

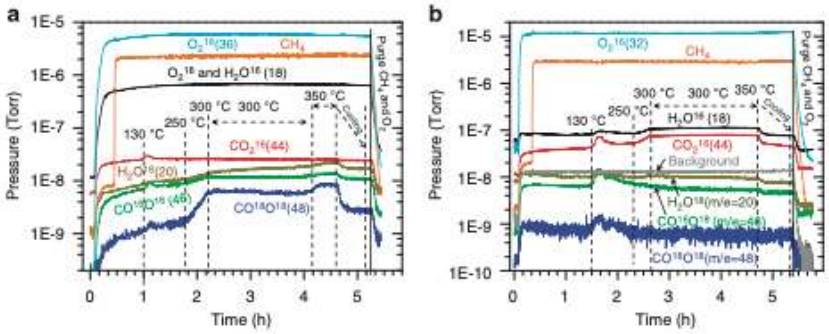

Figure 8 | Evolution of products. Evolution of products during (**a**) CH_4 complete oxidation in O_2^{18} on $NiCo_2O_4^{16}$, and (**b**) CH_4 complete oxidation in O_2^{16} on isotope-labelled catalyst $NiCo_2O_{4-x}^{16}O_x^{18}$ along the increase of catalysis temperature.

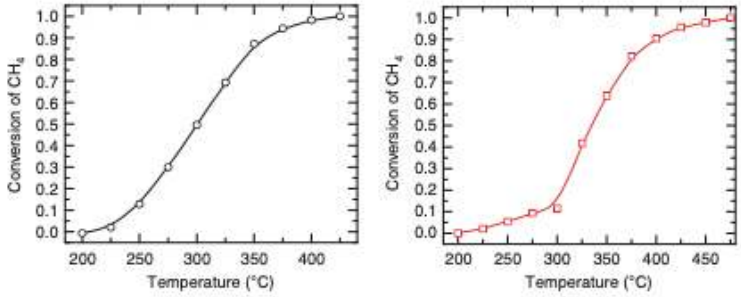

Figure 9 | Catalytic performance of $NiCo_2O_4$ in mixture of gases of exhaust of engines of natural gas vehicles. (**a**) Gas composition, CH_4: 0.2%, O_2: 5%, CO_2: 15%, H_2O: 10%, Ar: 69.8%. (**b**) Gas composition: CH_4: 0.2%, O_2: 5%, NO: 0.15%, H_2O: 10%, Ar: 69.8%. Flow rate of the mixture: 200 ml min^{-1}, amount of catalyst: 200 mg.

Upon the preparation, O_2^{18} was purged and a UHV environment (3×10^{-9} torr) was achieved before $NiCo_2O_{4-x}^{16}O_x^{18}$ was transformed to the reaction cell of AP-XPS. Then, combustion of CH_4 was performed on this isotope-labeled catalyst in *pure* O_2^{16} in the reaction cell of AP-XPS. The evolution of partial pressure of the three potential products $CO^{16}O^{16}$ (M/z = 44), $CO^{16}O^{18}$ (M/z = 46), and $CO^{18}O^{18}$ (M/z = 48) were recorded with the mass spectrometer (Fig. 8b). It is noted that $CO^{16}O^{18}$ (M/z = 46) was produced even at a relatively low temperature 130–150 °C; However, the partial pressure of $CO^{16}O^{18}$ (M/z = 46) decreased to its base line at a temperature higher than 150 °C. The decrease of $CO^{16}O^{18}$ partial pressure results from that fact that the source of O^{18} atoms in the isotope-labelled catalyst $NiCo_2O_{4-x}^{16}O_x^{18}$ is limited. The observation of $CO^{16}O^{18}$ shows that the surface lattice oxygen atoms directly participate into the formation of intermediate towards formation of product molecules.

Catalytic performance for removal of CH_4 in gas exhaust. To examine the catalytic performance of $NiCo_2O_4$ in a complete oxidation of CH_4 of gas exhaust of an engine of natural gas, we measured catalytic performance of a complete oxidation of CH_4 on $NiCo_2O_4$ in two different mixtures with gas compositions (Fig. 9) similar to the exhaust of lean-burn natural gas engine: (1) CH_4 0.2%, O_2 5%, CO_2 15%, H_2O 10% balanced with Ar with a flow rate of 200 ml min^{-1} (Figs 9a), and (2) CH_4 0.2%, O_2 5%, NO 0.15%, H_2O 10% balanced with Ar (Fig. 9b). These gas compositions are typically used in the evaluation of catalytic performance of Pd- and Pt-based catalysts for a complete oxidation of CH_4 in the exhaust of engines of natural gas[11–13]. In the mixture of CH_4 0.2%, O_2 5%, CO_2 15% and H_2O 10%, balanced with Ar, CH_4 can be completely oxidized to CO_2 and H_2O on 200 mg $NiCo_2O_4$ at 425 °C (Fig. 9a). Compared with 200 mg of $NiCo_2O_4$, 200 mg of 2.2wt%Pd/Al_2O_3 can completely oxidize the mixture of 0.2% CH_4, O_2 5%, CO_2 15% and H_2O 10% at 500 °C or higher[11]. Thus, $NiCo_2O_4$ exhibits higher activity than Pd/Al_2O_3 in the complete oxidation of CH_4 of exhaust gas in the temperature range of 400–500 °C. In the case of CH_4 0.2%, O_2 5%, NO 0.15% and H_2O 10% balanced with Ar, CH_4 can be oxidized completely to CO_2 and H_2O at 475 °C, while 200 mg $NiCo_2O_4$ is used (Fig. 9b). As the cost of Pd per kg is largely

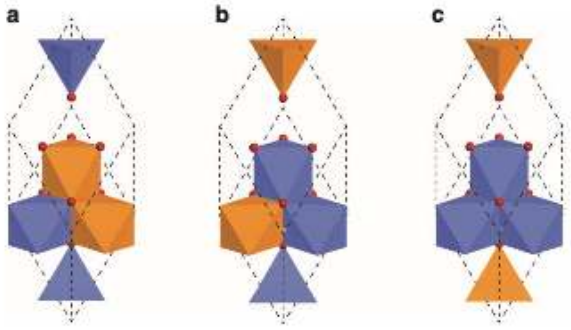

Figure 10 | Primitive cells of three different $NiCo_2O_4$ crystals. Nickel, cobalt and oxygen are shown in orange, blue and red, respectively. (**a**) Two Co^{3+} cations are substituted with two Ni^{3+}. (**b**) One Co^{3+} and one Co^{2+} cations are substituted with one Ni^{3+} and one Ni^{2+}, respectively. (**c**) Two Co^{2+} cations are substituted with two Ni^{2+}.

higher than nickel oxide and cobalt oxide by >3,000 times, the cost of raw materials of $NiCo_2O_4$ is <1% of the catalyst 2.2wt%Pd/Al_2O_3. Thus, $NiCo_2O_4$ is more active and certainly cost-effective compared with Pd/Al_2O_3 or Pt/Al_2O_3.

Crystal structures. The $NiCo_2O_4$ crystal structure was built by substituting Ni with Co in Co_3O_4 crystal structure. As shown in Fig. 10, three different substitution models of crystals were tested in our calculations, namely substituting two Co^{3+} with two Ni^{3+} (type I, Fig. 10a), substituting one Co^{3+} and one Co^{2+} with one Ni^{3+} and one Ni^{2+}, respectively (type II, Fig. 10b), and two Co^{2+} with two Ni^{2+} (type III, Fig. 10c). The type I crystal structure was found to be the most stable in our calculations, while the type II was slightly less stable by 0.01 eV per unit cell higher in energy. The type III was most unfavourable thermodynamically, 0.20 eV higher per unit cell than that of type I. In the following calculations, types I and II were considered.

Stabilities of different facets. Four different surfaces namely $NiCo_2O_4(100)$, $NiCo_2O_4(110)$-A, $NiCo_2O_4(110)$-B and $NiCo_2O_4(111)$, were chosen for both type I and type II crystals based on the X-ray diffraction results and our previous work on Co_3O_4 (ref. 29). The optimized structures were shown in Supplementary Fig. 11 and Supplementary Fig. 12. The surface energies of all the eight surfaces were listed in Supplementary Table 1. For both type I and type II crystals, (110)-A and (110)-B surfaces exhibit slightly higher surface energies by 0.02 or 0.03 eV than (100). (110)-A, (110)-B, and (100) of types I and II crystals with relatively low surface energies were considered in the following studies of surface reactivities.

Reactivities of different facets. To examine the reactivities of (110)-A, (110)-B, and (100) of type I and II crystals, the dissociations of the first C–H of CH_4 on these surfaces were investigated. Activation energies of these dissociations were listed in Supplementary Table 2. Transition states for these dissociations were presented in Supplementary Fig. 13 and Supplementary Fig. 14. These calculations (Supplementary Table 2) suggest that the 110-B of type I crystal are the most active for CH_4 activation on Ni^{3+} with lowest activation energy of only 0.52 eV which is lower than those on Ni(111) (0.88 eV)[30], Ni(211) (0.61 eV)[30] and Pd(100) (0.79 eV)[31]. Therefore, the low barrier on 110-B of type I crystal is responsible for the high reactivity of $NiCo_2O_4$ catalyst.

Active sites for dissociation of the first C–H of CH_4. To assign the sites for dissociation of CH_4 to CH_3, the binding strengths of CH_3 on cobalt and nickel sites of $NiCo_2O_4(110)$-B surfaces of both type I and type II crystals were calculated (Supplementary Table 3). The adsorption energies of CH_3 on nickel sites of (110)-B are stronger than those on cobalt sites for both types of crystals. In addition, as shown in Supplementary Table 2 the activation barrier for dissociation of CH_4 to CH_3 on Ni^{3+} of the most active surface $NiCo_2O_4$ (110-B) of crystal type I is much lower than Co^{3+} of this surface.

These DFT calculations suggest that Ni^{3+} cations are the sites for activating the first C–H of CH_4. This is consistent with experimental observation. *In situ* studies of $Ni_{0.75}Co_{2.25}O_{4-x}$ and $Ni_{1.25}Co_{1.75}O_{4-x}$ with AP-XPS were performed under the same catalytic condition as $NiCo_2O_{4-x}$. In these parallel experiments, the atomic fraction of Ni cations to the total of Ni and Co cations on the catalyst surface during catalysis was measured. As shown in Supplementary Fig. 15, the actual fractions of Ni cations on surfaces of $Ni_{0.75}Co_{2.25}O_{4-x}$, $NiCo_2O_{4-x}$, and $Ni_{1.25}Co_{1.75}O_{4-x}$ are 0.33, 0.51 and 0.44 at 250 °C, respectively. The conversions on $Ni_{0.75}Co_{2.25}O_{4-x}$, $Ni_1Co_2O_{4-x}$, and $Ni_{1.25}Co_{1.75}O_{4-x}$ at 275 °C are 10%, 27% and 17% (Supplementary Figure 16), respectively. The correlation between atomic fractions of Ni cations in Supplementary Fig. 15 and the catalytic conversion presented in Supplementary Fig. 16 shows that a higher atomic fraction of Ni cations on surface of a $Ni_xCo_{3-x}O_4$ catalyst offers higher conversion of CH_4. It further suggests that Ni cations instead of Co cations are active sites for activating C–H of CH_4.

Mechanism of complete oxidation of CH_4 on $NiCo_2O_4$. To fully understand the mechanism of CH_4 complete oxidation on $NiCo_2O_4$, a systematic investigation of potential reaction pathways was carried out on the most active surface, (110-B) of type I crystal of $NiCo_2O_4$. After the dissociation of CH_4 to CH_3, there are two different possibilities for the next elementary steps: a further dissociation of CH_3 into CH_2 (called dehydrogenation in Supplementary Fig. 17) or a coupling of carbon atom of CH_3 with oxygen atom of surface lattice (called oxidation in Supplementary Fig. 17). In order to determine which step is more favourable, we calculated the activation energies and enthalpy change for the two potential steps. The calculated energy profiles and the corresponding geometries were shown in Supplementary Fig. 17. Upon the first C–H dissociation, CH_3 species is oxidized into CH_3O binding to a Ni cation. The thermodynamically and kinetically favourable oxidation step forms an intermediate, CH_3O. This is different from the continuous dehydrogenation of CH_3 on Pd surface[14]. This preference of oxidation to CH_3O instead of further dehydrogenation to CH_2 or CH species could be understood as follows: the low coordinated species, such as CH_2 or CH, need more than one binding sites to stabilize them; however the singly dispersed nickel cations on surface lattice of Co_3O_4 are not an adsorption site consisting of continuously packed Ni atoms for CH_2 or CH. Therefore, a further dehydrogenation of CH_3 to CH_2 to CH is a high endothermic step on $NiCo_2O_4$ compared with the pathway of oxidation.

Supplementary Figure 18 presents the two potential reaction pathways A and B after the formation of CH_3O species. DFT calculations show that pathway B is the preferred one. The following section will describe this preferred pathway. On the basis of the experimental results and previous calculations[29,32], CHO species plays very important roles in the oxidation of methane on many different catalyst surfaces; thus CH_3O could dehydrogenate to CH_2O and then CHO with a following oxidation to form product molecules.

For dehydrogenation of CH_3O to CHO, there are two different dehydrogenation pathways schematically shown in Supplementary Fig. 18: (i) the dehydrogenation of CH_3O by the OH species of nickel site (pathway A shown in red in Supplementary Fig. 18); (ii) the dehydrogenation by the O species of nearby cobalt site (pathway B shown in black in Supplementary Fig. 18). On the basis of the energy profiles of the two pathways in Supplementary Fig. 19a, pathway B is more favourable than pathway A, which suggests that the dehydrogenation of CH_3O by oxygen atoms (not shown) bonded to nearby cobalt site (pathway B) is preferred over a dehydrogenation of CH_3O by OH species bonded to nickel site (Supplementary Fig. 18) in the overall reaction (pathway A).

Transformation of intermediate CHO to product molecules. As mentioned above, the transformation of intermediate CHO to product molecules could go through a sub-pathway of OCHO dehydrogenation (marked with purple in the right panel of Supplementary Fig. 18) other than the sub-pathway of CO oxidation (marked with black in the right panel of Supplementary

Fig. 18). Supplementary Figure 21a shows the two sub-pathways considered in our DFT calculations. Our DFT calculations revealed that each sub-pathway includes two steps with two transition states and one intermediate. OCHO is the intermediate of the sub-pathway of OCHO dehydrogenation (Supplementary Fig. 21).

In the sub-pathway of OCHO dehydrogenation (red in Supplementary Fig. 21a,b), the CHO couples with oxygen atom and thus forms an intermediate OCHO (the first step in transforming CHO to product molecules); then the intermediate OCHO is dehydrogenated to CO_2 (the second step); it is quite different from the sub-pathway of CO oxidation (black line in Supplementary Fig. 21a,b). We calculated the sub-pathway of OCHO dehydrogenation for transforming CHO to product molecules. The calculated energy profiles of the two sub-pathways were presented in Supplementary Fig. 21b. The geometries of transition states and intermediates of the sub-pathways of OCHO dehydrogenation and CO oxidation were presented in Supplementary Fig. 21c and Supplementary Fig. 21d, respectively.

From the calculated energy profiles presented in Supplementary Fig. 21b, several interesting features were found. The barrier of the first transition state in the sub-pathway of OHCO dehydrogenation (red line in Supplementary Fig. 21b) is lower than that of the first barrier in the sub-pathway of CO oxidation (black line in Supplementary Fig. 21b); in addition, the OCHO intermediate in the sub-pathway of OCHO dehydrogenation is more thermodynamically stable than the intermediate of the sub-pathway of CO oxidation by 0.63 eV. Thus, the formation of OCHO intermediate is thermodynamically and kinetically favourable. However, the barrier for transforming OCHO intermediate to CO_2 is higher than the second barrier of the sub-pathway of CO oxidation (Supplementary Fig. 21b). Therefore, the formed OCHO intermediate could be experimentally observed at a relatively low temperature. In fact, our *in situ* studies of the catalyst surface in the mixture of CH_4 and O_2 with AP-XPS did identify the intermediate OCHO at a temperature lower than 200 °C; the C 1*s* photoemission feature of this intermediate is at 288.3 eV which is consistent with the OCHO species reported in literature[25]. In addition, the observed vibration signatures of this intermediate at 1,280, 1,430, and 1,561 cm^{-1} *in situ* infrared studies (Fig. 6) at 160 °C are consistent with the OCHO species formed in water–gas shift.[25]

In the sub-pathway of OCHO dehydrogenation, the second step (from OCHO intermediate to product molecules shown in red line in Supplementary Fig. 21b) is highly exothermic with a free energy change of −3.50 eV. Therefore, at high temperature the OCHO intermediate can readily overcome the barrier and transform to product molecule CO_2, driven by the thermodynamics factor although the barrier of the second transition state is relatively high compared with the second one in the sub-pathway of CO oxidation. In fact, the evolution of C 1*s* photoemission feature at 288.3 eV during catalysis from low temperature to high temperature shows that this intermediate OCHO disappears at about 200 °C along the increase of catalysis temperature (Fig. 4d).

Discussion

In situ studies using ambient pressure photoelectron spectroscopy, vibrational spectroscopy, and isotope-labelled experiments show that (1) molecular O_2 dissociates on surface oxygen vacancies; (2) the dissociated oxygen atoms fill in oxygen vacancies and couple with hydrogen atoms dissociated from intermediate to from OH and then H_2O molecules; (3) CH_4 dissociates on Ni cations to form CH_3 with a following oxidation to CH_3O; (4) intermediate CHO is formed through dehydrogenation of CH_3O with oxygen species of nearby cobalt site; (5) CHO is transformed to CO_2 and H_2O through two sub-pathways termed OCHO dehydrogenation and CO oxidation. Due to high activity and low cost of $NiCo_2O_4$ catalyst in completely oxidizing CH_4 to CO_2 and H_2O at a relatively low temperature, $NiCo_2O_4$ is a very promising catalyst for removing CH_4 of gas exhaust of natural gas engine through a complete oxidation.

The mechanisms of methane oxidation on $NiCo_2O_4$(100)-B are different from those on metal surfaces[14,30,32]. For instance, CH_4 on metal surfaces sequentially and continuously dehydrogenates to CH species and then is oxidized to an intermediate CHO, while our studies suggest that after dissociation of first C–H in methane, the CH_3 species will couple with oxygen atom of the lattice oxygen, forming CH_3O species. The lack of direct dehydrogenation of CH_3 to CH_2 and then to CH on $NiCo_2O_4$ likely results from the low binding energy of CH_2 or CH species on isolated Ni cations anchored on surface lattice of Co_3O_4. In other words, the separated Ni cation sites could not stabilize the low coordinate species such as CH_2 and CH. In these calculated pathways on the $NiCo_2O_4$(100)-B, the surface lattice oxygen atom in the nearby cobalt sites was found to be very important in the dehydrogenation of CH_3O.

Computational studies suggest that the pathways from transferring CHO to CO_2 are different from that on metal surface[14,33,34]. Sub-pathway of CO oxidation and sub-pathway of OCHO dehydrogenation were both proposed for the transformation of CHO intermediate to CO_2. CO oxidation sub-pathway was found more kinetically favourable in the second elemental step (Supplementary Fig. 21b). Furthermore, the OCHO intermediate (red in Supplementary Fig. 21) was found to be stable at low temperature due to the high activation barrier (1.64 eV) for transforming the intermediate OCHO to product molecules. However, this intermediate (OCHO) is unstable at high temperature due to the exothermic nature of the transformation from OCHO intermediate to CO_2 (Supplementary Fig. 21b). Compared to the intermediate of the sub-pathway of CO oxidation, the higher thermodynamic stability of OCHO intermediate of the sub-pathway of OCHO dehydrogenation and its kinetically unfavourable transformation to CO_2 make it observable at a relatively low temperature.

Methods

Synthesis. $NiCo_2O_4$, $Ni_{1.25}Co_{1.75}O_4$ and $Ni_{0.75}Co_{2.25}O_4$ nanoparticles were all synthesized through a co-deposition precipitation and a following thermal decomposition. The chemicals $Co(NO_3)_2 \cdot 6H_2O$ (≥98%), $Ni(NO_3)_2 \cdot 6H_2O$ (≥97%), and KOH (≥85%) were purchased from Sigma-Aldrich and were used as received. 0.01 mol $Ni(NO_3)_2 \cdot 6H_2O$, and 0.02 mol $Co(NO_3)_2 \cdot 6H_2O$ were physically mixed and completely dissolved in 50 ml deionized water. Then 150 ml KOH (1 M) was added under the bubbling of N_2 and with continuously stirring. During this process the temperature was kept at room temperature. A blue colloidal solution was obtained after the introduction of KOH. A dark blue precipitate was collected on centrifuging the prepared solution. Then, the dark blue precipitate was first washed with hot deionized water (60 °C) for several times with a following drying at 130 °C for 24 h. The obtained black solid was grounded to powder and was further calcined at 350 °C in air for 24 h, forming the as-synthesized catalyst $NiCo_2O_4$. To synthesize $Ni_{0.75}Co_{2.25}O_4$ and $Ni_{1.25}Co_{1.75}O_4$, the method is almost the same as the one for the synthesis of $NiCo_2O_4$. For synthesis of $Ni_{1.25}Co_{1.75}O_4$, 0.0125 mol $Ni(NO_3)_2 \cdot 6H_2O$, and 0.0175 mol $Co(NO_3)_2 \cdot 6H_2O$ were used. 0.0075 mol $Ni(NO_3)_2 \cdot 6H_2O$ and 0.0225 mol $Co(NO_3)_2 \cdot 6H_2O$ were used for the synthesis of $Ni_{0.75}Co_{2.25}O_4$.

Structural characterization. Powder X-ray diffraction patterns of $NiCo_2O_4$, $Ni_{1.25}Co_{1.75}O_4$, and $Ni_{0.75}Co_{2.25}O_4$ nanocatalysts were collected on a Bruker D8 advance XRD using nickel-filtered Cu Kα radiation ($\lambda = 1.54056$ Å). The measurements were operated at 40 kV and 40 mA in a continuous mode with the scanning rate of 4.2° min^{-1} in the 2θ range from 10° to 80°.

The size, shape and lattice fringe of catalysts were identified by high-resolution transmission electron microscope (FEI, Titan 80 – 300) operated at an accelerating voltage of 200 kV or lower. Image analysis was performed with Digital Micrograph

(Gatan) software. The catalyst samples for TEM characterization were prepared by dropping their colloidal solutions onto copper grids supported on carbon films.

***In situ* studies of catalysts under reaction conditions and during catalysis.** The *in situ* characterizations of surface chemistry of $NiCo_2O_4$, $Ni_{0.75}Co_{2.25}O_4$, and $Ni_{1.25}Co_{1.75}O_4$ nanocatalysts during catalysis were performed on the in-house AP-XPS system. Monochromated Al Kα line was used as X-ray source. Unlike traditional UHV studies, in AP-XPS studies reactant gases are introduced to continuously flow through the catalyst at a desired temperature in the reaction cell while data acquisition is going on. Thus, the *in situ* study is defined to be a study in which the measurement of catalyst surface or adsorbate is being performed, while a catalyst is buried in gas reactant (s). The *in situ* characterization of AP-XPS[22,35,36] could be different from the *in situ* studies defined in other places since sometimes *in situ* study is defined as a characterization of a sample without changing location/position after a sample preparation or vapour deposition.

The reaction cell was incorporated into the UHV chamber of AP-XPS system. Gas flows through the cell and exits through the exit port and an aperture that interfaces the gaseous environment in the reaction cell and vacuum environment of the prelens. Flow rate in the reaction cell was measured through a mass flow metre installed before the entrance of the reaction cell. In this study, the typical flow rate of pure gas is in the range of 3–5 ml min^{-1}. As the gas source used in AP-XPS studies is pure gas, 3–5 ml min^{-1} equals to 60–100 ml min^{-1} of 5% reactant gas used in catalytic measurements in a fixed-bed flow reactor. The total pressure of the mixture gas at the entrance is measured with a capacitance gauge, while the pressure at the exit is measured with another capacitance gauge. An average of the pressures at entrance and exit is defined to be the pressure above the catalyst in the reaction cell. An external heating source in the UHV environment heats the catalyst in the environment of reactant gases in the reaction cell. More detailed description of the in-house AP-XPS system can be found in our previous publications[20].

To avoid surface charging, we use Au, Ag, or HOPG to load catalysts for AP-XPS studies and control the thickness of catalyst layer on a surface[19,37,38]. In this work, we use Au foil as the substrate to physically load a thin layer of nanocatalysts. The Au foil is deliberately roughened using a SiC knife to increase the adhesion for loading. The apparent binding energies of Au 4*f*, Ni 2*p*, Co 2*p*, and O 1*s* of sample prepared on the Au substrate are very close to their real values, suggesting there is no identifiable surface charging. All XPS spectra are calibrated to their corresponding Au $4f_{7/2}$ binding energy which is at 84.0 eV. Analyses of XPS peaks are performed with Casa XPS program.

In situ infrared studies are performed in a reaction cell filled with 1 bar reactant gas at Oak Ridge National Lab. This reaction cell can be heated up to high temperatures. The same catalytic condition as measurements of catalytic performances was used in the infrared studies.

On-line observation of products at different temperatures. Our in-house AP-XPS system also allows us to monitor the change of the gas composition during catalysis with a quadrupole mass spectrometer. Three differential pumping stages were installed between the reaction cell and the energy analyser. The aperture mounted on the reaction cell separates the high-pressure environment of the reaction cell from the vacuum of the first differential pumping stage (prelens), and also allows for leaking gases on the reaction cell into the differential pumping stages. The analyses of gas composition at different temperatures during catalysis were done by a quadrupole mass spectrometer, which is mounted at the second differential pumping stage of the AP-XPS system. To exclude the possibility that gas expansion at a high temperature or fast diffusion of molecules from reaction cell of AP-XPS to UHV chamber of mass spectrometer results in an increase of partial pressure of product molecules, Ar gas was introduced as a reference gas (background) to the reaction cell. No change in the partial pressure of Ar along with the increase of temperature of catalysts shows that the increase of partial pressure of CO_2 and H_2O is not due to thermal expansion of gas at a relatively high temperature.

Such an on-line analysis of gas composition (reactants and products) in the reaction cell of AP-XPS allows for building a simultaneous correlation between the products and real-time surface chemistry of catalysts at different catalysis temperatures. The on-line mass spectroscopy experiments allow for tracking evolution of different products at different temperatures formed through isotope-labeled catalysts $NiCo_2O_{4-x}^{16}O_x^{18}$ or through using isotope-labelled reactant O_2^{18} during data acquisition of in-situ AP-XPS studies.

Measurements of catalytic performance. The catalytic performance was measured in a fixed-bed tubular quartz micro flow reactor (inner diameter = 6 mm, length = 300 mm), at atmospheric pressure. The catalyst (25–500 mg) was sieved (40–60 mesh) and loaded into the reactor between two layers of quartz sands, packed in between two quartz wool plugs. The catalyst was heated in a furnace equipped with a proportional-integral-derivative temperature controller. The temperature of the catalyst was measured with a K-type thermocouple inserted into the reactor and touching the catalyst bed.

The reactant gas composition was controlled by varying the flow rates of CH_4 mixture (10% CH_4 balanced in Ar) and O_2 (pure O_2). The flow rate of CH_4 mixture (10% balanced in Ar) and O_2 (pure) was precisely controlled through their own mass flow metres (Dakota Instruments, Inc.). When vary the flow rate of CH_4 mixture and O_2, the ratio of pure CH_4 to pure O_2 was always keeping at 1:5. The typical flow rate of CH_4 mixture (10% balanced in Ar) is 100 ml min^{-1}, while the flow rate of O_2 (pure) is 50 ml min^{-1}. The reliability of the fix-bed reactor was checked through a blank experiment with the same experimental parameters including reactant gases, flow rate and reaction temperature. In the blank experiment, only silica supporting material was loaded in the reactor. No appreciable conversion of CH_4 was found in the blank experiment in the temperature range of 25–800 °C.

The effluent gas was connected to a gas chromatograph equipped with a HayeSep D (6′ × 1/8″) packed column, a molecular sieve 13 × (6′ × 1/8″) packed column, and a thermal conductivity detector (TCD) for analysis of both reactants and products. The CH_4 conversion X% was defined as: $X\% = \left[\left(mol_{CH_4,inlet} - mol_{CH_4,outlet}\right)/mol_{CH_4,inlet}\right] \times 100$. Herein, $mol_{CH_4,inlet}$ and $mol_{CH_4,outlet}$ are the amounts of pure CH_4 at the inlet and outlet of the reactor, respectively. In the CH_4 combustion reaction, $mol_{CH_4,inlet}$ and $mol_{CH_4,outlet}$ can be directly represented by the peak area of CH_4 in gas chromatograph before reaction and after reaction, respectively.

Computational studies. In this work all the DFT calculations were carried out with a periodic slab model using the Vienna *ab initio* simulation program[33,39–41]. The generalized gradient approximation was used with the Perdew-Burke-Ernzerhof[42] exchange-correlation functional. Due to the strong correlation effect among the partially filled Co 3*d* states, we used the Hubbard parameter, U, for the Co 3*d* electrons to take the on-site Coulomb interaction into account, which is the well-known DFT + U method[34]. According to previous work[29,43], the value of U-J of 2 eV was applied. The projector-augmented wave method[44,45] was utilized to describe the electron-ion interactions, and the cut-off energy for the plane-wave basis set was 400 eV. Brillouin zone integration was accomplished using a 2 × 2 × 1 Monkhorst-Pack k-point mesh. All the adsorption geometries were optimized using a force-based conjugate gradient algorithm, while transition states were located with a constrained minimization technique[46–48].

References

1. Zarur, A. J. & Ying, J. Y. Reverse microemulsion synthesis of nanostructured complex oxides for catalytic combustion. *Nature* **403,** 65–67 (2000).
2. Cargnello, M. *et al.* Exceptional Activity for Methane Combustion over Modular Pd@CeO2 Subunits on Functionalized Al2O3. *Science* **337,** 713–717 (2012).
3. Farrauto, R. J. Low-temperature oxidation of methane. *Science* **337,** 659–660 (2012).
4. Andrushkevich, T. V., Boreskov, G. K., Popovskii, V., Muzikantov, V., Kimhai, O. & Sazonov, V. *Kinet. Katal* **9,** 595 (1968).
5. Andrushkevich, T. V., Boreskov, G. K., Popovskii, V., Pliasova, L., Karakchiev, L. & Ostankovitch, A. *Kinet. Katal* **9,** 1244 (1968).
6. Papadato, K & Shelstad, K. A. Catalyst screening using a stone DTA apparatus .1. oxidation of toluene over cobalt-metal-oxide catalysts. *J. Catal.* **28,** 116–123 (1973).
7. Baussart, H., Delobel, R., Lebras, M. & Leroy, J. M. Oxidation of propene on mixed oxides of copper and cobalt. *J. Chem. Soc. Farad. T I* **75,** 1337–1345 (1979).
8. Prasad, R., Sony & Singh, P. Low temperature complete combustion of a lean mixture of LPG emissions over cobaltite catalysts. *Catal. Sci. Technol.* **3,** 3223–3233 (2013).
9. Gelin, P. & Primet, M. Complete oxidation of methane at low temperature over noble metal based catalysts: a review. *Appl. Catalys. B Environ.* **39,** 1–37 (2002).
10. Samsa, M. E. *Potential for Compressed Natural Gas Vehicles in Centrally-Fueled Automobile, Truck and Bus Fleet Applications* (Gas Research Institute, Chicago, IL, 1991).
11. Gelin, P., Urfels, L., Primet, M. & Tena, E. Complete oxidation of methane at low temperature over Pt and Pd catalysts for the abatement of lean-burn natural gas fuelled vehicles emissions: influence of water and sulphur containing compounds. *Catalys. Today* **83,** 45–57 (2003).
12. Honkanen, M. *et al.* Structural characteristics of natural-gas-vehicle-aged oxidation catalyst. *Top. Catal.* **56,** 576–585 (2013).
13. Lampert, J. K., Kazi, M. S. & Farrauto, R. J. Palladium catalyst performance for methane emissions abatement from lean burn natural gas vehicles. *Appl. Catal. B Environ.* **14,** 211–223 (1997).
14. Chin, Y.-H., Buda, C., Neurock, M. & Iglesia, E. Consequences of metal–oxide interconversion for C–H bond activation during CH4 reactions on Pd catalysts. *J. Am. Chem. Soc.* **135,** 15425–15442 (2013).
15. Zhang, S. R. *et al.* WGS Catalysis and In Situ Studies of CoO1-x, PtCon/Co3O4, and PtmCom '/CoO1-x Nanorod Catalysts. *J. Am. Chem. Soc.* **135,** 8283–8293 (2013).
16. Henrich, V. E., & Cox, P. A. *The Surface Science of Metal Oxides* (Cambridge Univ. Press, 1994).

17. Jiang, D. E. & Dai, S. The role of low-coordinate oxygen on Co3O4(110) in catalytic CO oxidation. *Phys. Chem. Chem. Phys.* **13,** 978–984 (2011).
18. Xie, X. W., Li, Y., Liu, Z. Q., Haruta, M. & Shen, W. J. Low-temperature oxidation of CO catalysed by Co3O4 nanorods. *Nature* **458,** 746–749 (2009).
19. Wang, L. *et al.* Catalysis and In-situ Studies of Rh1Con/Co3O4 Nanorods in Reduction of NO with H_2. *ACS Catalys.* **3,** 1011–1019 (2013).
20. Tao, F. Design of an in-house ambient pressure AP-XPS using a bench-top X-ray source and the surface chemistry of ceria under reaction conditions. *Chem. Commun.* **48,** 3812–3814 (2012).
21. Klissurski, D. G. & Uzunova, E. L. A comparative-study of the thermal-stability of nickel, copper and zinc spinel cobaltites. *Thermochim. Acta* **189,** 143–149 (1991).
22. Tao, F. *et al.* Reaction-Driven Restructuring of Rh-Pd and Pt-Pd Core-Shell Nanoparticles. *Science* **322,** 932–934 (2008).
23. Zhang, S. R. *et al.* Restructuring transition metal oxide nanorods for 100% selectivity in reduction of nitric oxide with carbon monoxide. *Nano Letters* **13,** 3310–3314 (2013).
24. Shan, J. J. *et al.* Catalytic performance and in situ surface chemistry of pure alpha-MnO2 nanorods in selective reduction of NO and N2O with CO. *J. Phys. Chem.* **117,** 8329–8335 (2013).
25. Mudiyanselage, K. *et al.* Importance of the metal-oxide interface in catalysis: *in situ* studies of the water-gas shift reaction by ambient-pressure X-ray photoelectron spectroscopy. *Angew. Chem. Int. Ed. Engl* **52,** 5101–5105 (2013).
26. Deng, X. Y. *et al.* Reactivity differences of nanocrystals and continuous films of alpha-Fe2O3 on Au(111) studied with in situ X-ray photoelectron spectroscopy. *J. Phys. Chem. C* **114,** 22619–22623 (2010).
27. Deng, X. Y. *et al.* Surface chemistry of Cu in the presence of CO2 and H2O. *Langmuir* **24,** 9474–9478 (2008).
28. Wang, W., Su, C., Wu, Y. Z., Ran, R. & Shao, Z. P. Progress in solid oxide fuel cells with nickel-based anodes operating on methane and related fuels. *Chem. Rev.* **113,** 8104–8151 (2013).
29. Wang, H.-F. *et al.* Origin of extraordinarily high catalytic activity of Co3O4 and its morphological chemistry for CO oxidation at low temperature. *J. Catal.* **296,** 110–119 (2012).
30. Wang, Z., Cao, X. M., Zhu, J. & Hu, P. Activity and coke formation of nickel and nickel carbide in dry reforming: a deactivation scheme from density functional theory. *J. Catal.* **311,** 469–480 (2014).
31. Zhang, C. J. & Hu, P. Methane transformation to carbon and hydrogen on Pd(100): Pathways and energetics from density functional theory calculations. *J. Chem. Phys.* **116,** 322–327 (2002).
32. Inderwildi, O. R., Jenkins, S. J. & King, D. A. Mechanistic studies of hydrocarbon combustion and synthesis on noble metals. *Angew. Chem. Int. Ed.* **47,** 5253–5255 (2008).
33. Kresse, G. & Hafner, J. Ab initio molecular dynamics for liquid metals. *Phys. Rev. B* **47,** 558–561 (1993).
34. Dudarev, S. L., Botton, G. A., Savrasov, S. Y., Humphreys, C. J. & Sutton, A. P. Electron-energy-loss spectra and the structural stability of nickel oxide:An LSDA + U study. *Phys. Rev. B* **57,** 1505–1509 (1998).
35. Tao, F. *et al.* Break-up of stepped platinum catalyst surfaces by high CO coverage. *Science* **327,** 850–853 (2010).
36. Tao, F. & Salmeron, M. *In situ* studies of chemistry and structure of materials in reactive environments. *Science* **331,** 171–174 (2011).
37. Zhang, S. *et al.* In-Situ Studies of Nanocatalysis. *Acc. Chem. Res.* **46,** 1731–1739 (2013).
38. Zhu, Y. *et al. In situ* surface chemistries and catalytic performances of ceria doped with palladium, platinum, and rhodium in methane partial oxidation for the production of syngas. *ACS Catal.* **3,** 2627–2639 (2013).
39. Kresse, G. & Furthmüller, J. Efficient iterative schemes for ab initio total-energy calculations using a plane-wave basis set. *Phys. Rev. B* **54,** 11169–11186 (1996).
40. Kresse, G. & Furthmuller, J. Efficiency of ab-initio total energy calculations for metals and semiconductors using a plane-wave basis set. *Comput. Mster. Sci.* **6,** 15–50 (1996).
41. Kresse, G. & Hafner, J. Ab-initio molecular-dynamics simulation of the liquid-metal amorphous-semiconductor transition in germanium. *Phys. Rev. B* **49,** 14251–14269 (1994).
42. Perdew, J. P., Burke, K. & Ernzerhof, M. Generalized gradient approximation made simple. *Phys. Rev. Lett.* **77,** 3865–3868 (1996).
43. Lv, C.-Q., Liu, C. & Wang, G.-C. A DFT study of methanol oxidation on Co3O4. *Catal. Commun.* **45,** 83–90 (2014).
44. Kresse, G. & Joubert, D. From ultrasoft pseudopotentials to the projector augmented-wave method. *Phys. Rev. B* **59,** 1758–1775 (1999).
45. Blöchl, P. E. Projector augmented-wave method. *Phys. Rev. B* **50,** 17953–17979 (1994).
46. Michaelides, A. *et al.* Identification of general linear relationships between activation energies and enthalpy changes for dissociation reactions at surfaces. *J. Am. Chem. Soc.* **125,** 3704–3705 (2003).
47. Liu, Z. P. & Hu, P. General rules for predicting where a catalytic reaction should occur on metal surfaces: A density functional theory study of C-H and C-O bond breaking/making on flat, stepped, and kinked metal surfaces. *J. Am. Chem. Soc.* **125,** 1958–1967 (2003).
48. Alavi, A., Hu, P. J., Deutsch, T., Silvestrelli, P. L. & Hutter, J. CO oxidation on Pt(111): An ab initio density functional theory study. *Phys. Rev. Lett.* **80,** 3650–3653 (1998).

Supplementary Information

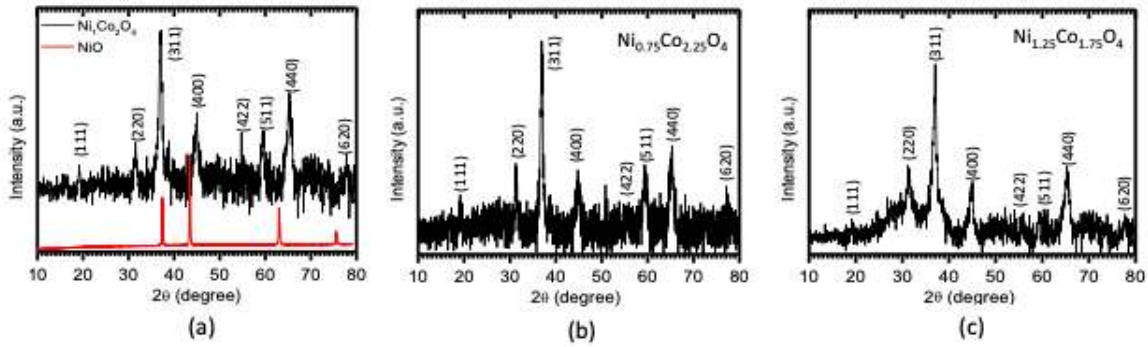

Supplementary Figure 1. XRD of $NiCo_2O_4$, $Ni_{0.75}Co_{2.25}O_4$, and $Ni_{1.25}Co_{1.75}O_4$. Diffraction pattern of NiO was included in Figure S1a for a comparison. Compared to NiO, the XRD patterns of the $NiCo_2O_4$, $Ni_{1.25}Co_{1.75}O_4$ and $Ni_{0.75}Co_{2.25}O_4$ are very different. Obviously, there is no NiO nanocluster formed in or on the three catalysts. More importantly, these three catalysts exhibit the exact same diffraction pattern as Co_3O_4, which suggests that theses catalysts have the same lattice as Co_3O_4.

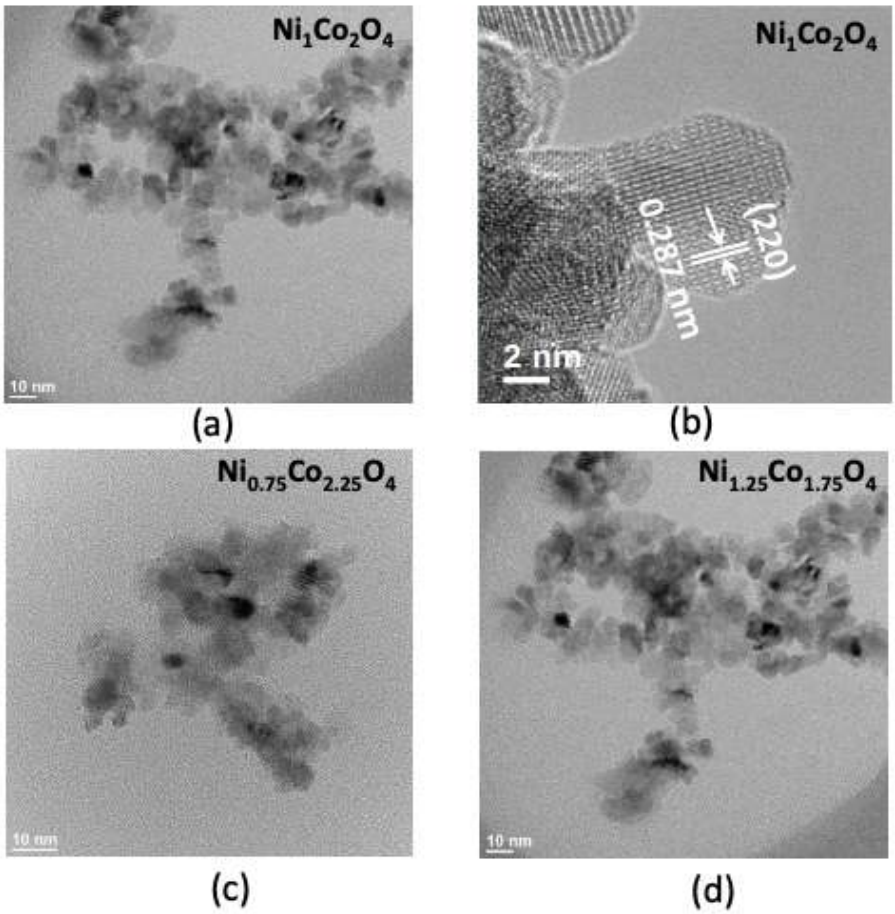

Supplementary Figure 2. TEM images of $NiCo_2O_4$, $Ni_{1.25}Co_{1.75}O_4$, and $Ni_{0.75}Co_{2.25}O_4$. These catalysts are nanoparticles with an average size of ~4.5 nm. The inter-planar distance measured from the fringe of high-resolution images is 0.287 nm along [110] direction. It is consistent with the crystallographic lattice constant of Co_3O_4. The TEM studies suggest the formation of the same crystallographic lattice as spinel Co_3O_4.

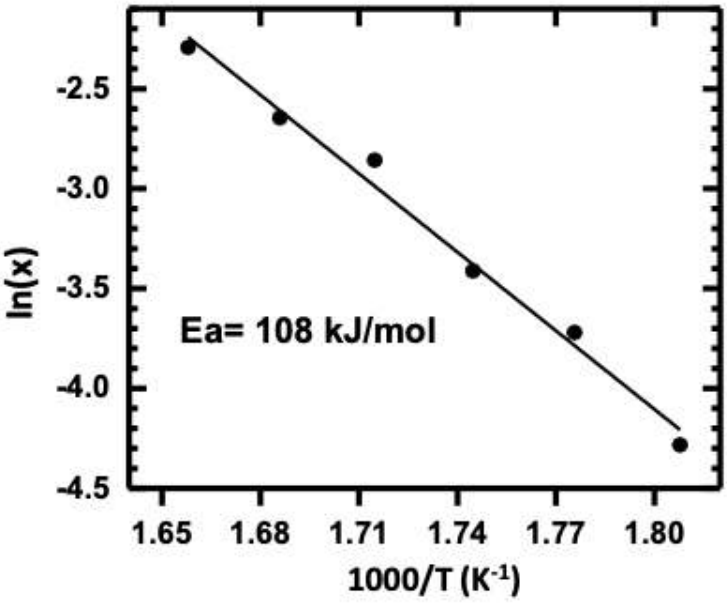

Supplementary Figure 3. Kinetic studies of the complete oxidation of methane at kinetics control regime (conversion < 10%). The Arrhenius plot of lnX to $\frac{1000}{T}$ (X is the conversion; T is catalysis temperature in Kevin) allows for calculation of activation energy. The calculated activation barrier is about 108 kJ/mol. 25 mg $NiCo_2O_4$ was used for kinetics; 100 ml/min 10% CH_4 and 50 ml/min 99.9% O_2 were introduced.

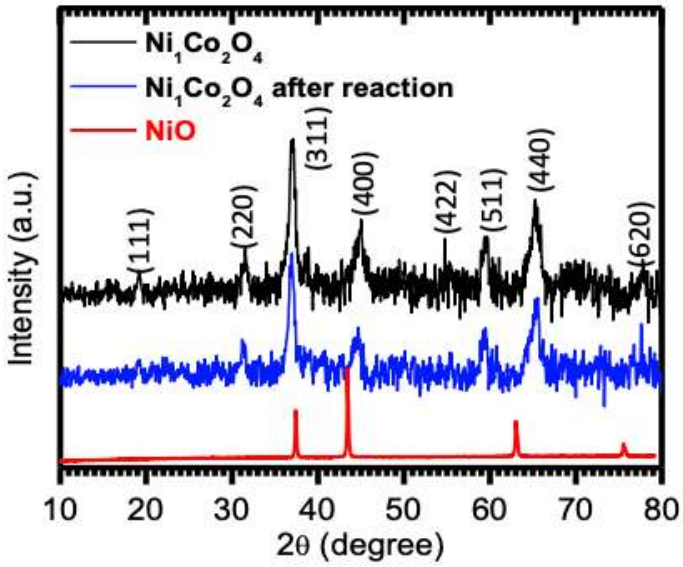

Supplementary Figure 4. XRD patterns of pure NiO (red), $NiCo_2O_4$ before catalysis (black), and $NiCo_2O_4$ after catalysis at 550°C (blue).

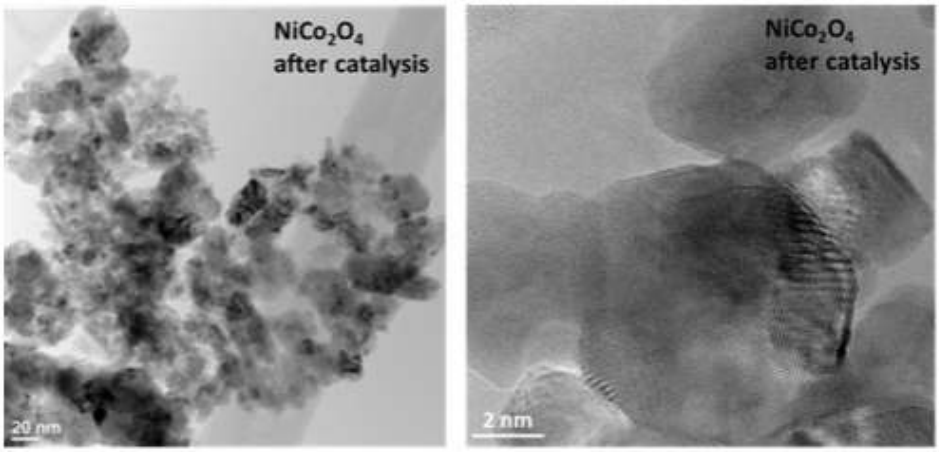

Supplementary Figure 5. TEM studies of $NiCo_2O_4$ catalyst before and after catalysis. (a) Large-scale TEM image of $NiCo_2O_4$ before catalysis and (b) high-resolution TEM image of $NiCo_2O_4$ after catalysis at 550°C. There is no obvious aggregation upon the catalysis at 550°C.

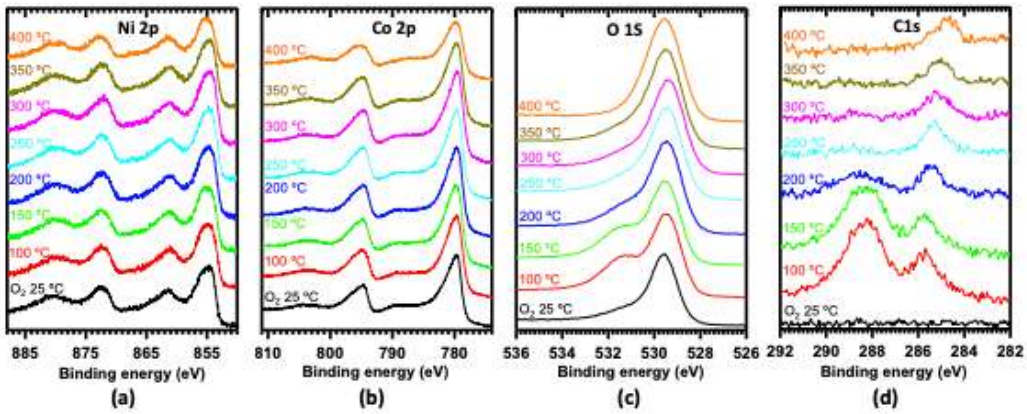

Supplementary Figure 6. Ni 2p (a), Co 2p (b), O 1s (c), and C 1s (d) of $Ni_{0.75}Co_{2.25}O_4$ during in-situ studies using AP-XPS. Obviously, its photoemission features are very similar to $NiCo_2O_4$ in Figure 4.

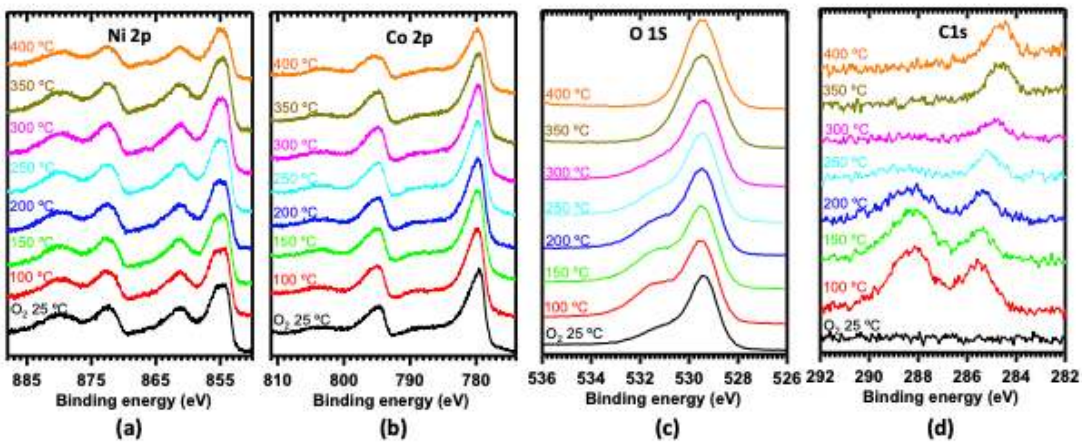

Supplementary Figure 7. Ni 2p (a), Co 2p (b), O 1s (c), and C 1s (d) of $Ni_{1.25}Co_{1.75}O_4$ during in-situ studies using AP-XPS. Obviously, $Ni_{1.25}Co_{1.75}O_4$ exhibits photoemission features very similar to $NiCo_2O_4$ in Figure 4.

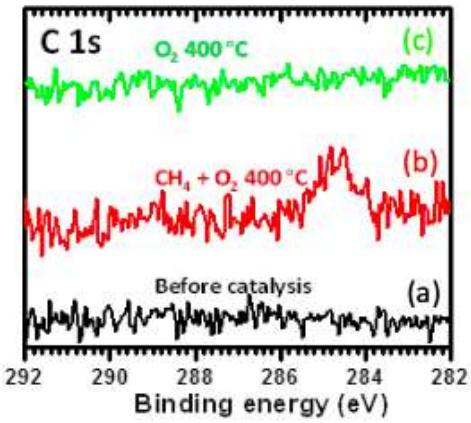

Supplementary Figure 8. C 1s of (a) surface of $NiCo_2O_4$ before introduction of CH_4 and O_2, (b) surface of $NiCo_2O_4$ during catalysis in the mixture of CH_4 and O_2 at 400°C, and (c) surface of $NiCo_2O_4$ in pure O_2 after CH_4 was purged but O_2 kept in the reaction cell. The disappearance of the C 1s photoemission feature at 284.6 eV in a few minutes shows that oxygen atoms continuously reacted with the CH_n species (formed on the catalyst surface) at 400°C to form CO_2 and thus the carbon species of peak 1 disappeared. It clearly shows that the surface carbon-containing species of peak 1 of the C 1s in Figure 4 are not any accumulated carbon layers as it can be readily oxidized to CO_2 in minutes.

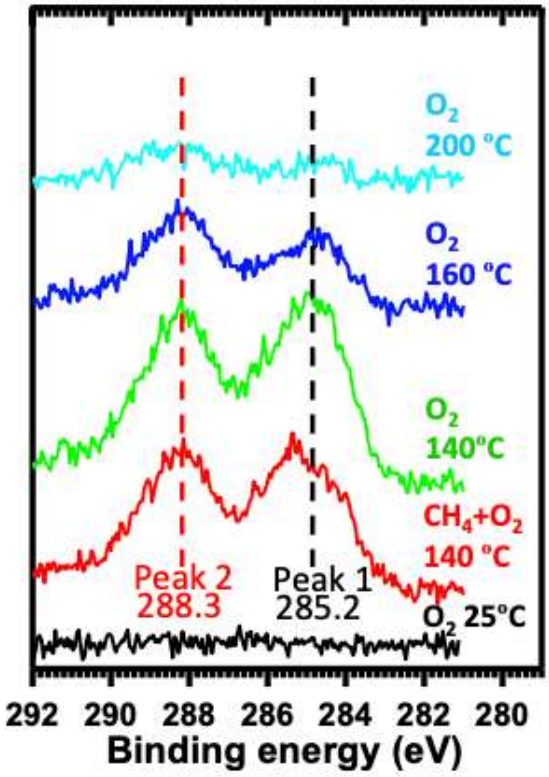

Supplementary Figure 9. C 1s spectra as a function of reaction conditions. Before catalysis, there are no carbon atoms on surface (black line). Upon introduction of CH_4 and O_2 and anneal to 140°C, peaks 1 and 2 are observed, assigned to CH_n species and OCHO intermediates, respectively. Upon closing the flow of CH_4 and remaining O_2, intensity of the two C 1s peaks decreased. At 200°C in O_2, both peaks 1 and 2 of C1s disappear due to the formation of CO_2. The ready oxidation of carbon species of peak 1 to CO_2 at 200°C shows that the carbon-containing species of peak 1 of C 1s is not contributed from any accumulated carbon layers since it can be oxidized to CO_2 at a temperature of only 200°C.

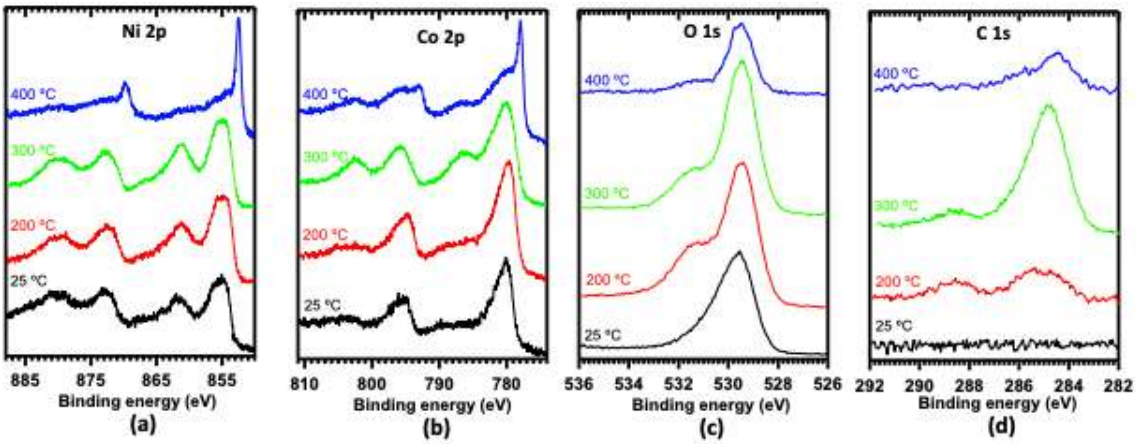

Supplementary Figure 10. Photoemission features of Ni 2p (a), Co 2p (b), O 1s (c), and C 1s (d) of $NiCo_2O_4$ as a function of temperature in the presence of pure CH_4 in the Torr range. There is no O_2 in these in-situ AP-XPS studies. Obviously, nickel cations and cobalt cations were reduced to metallic nickel and cobalt at 400°C by hydrogen atoms dissociated from CH_4. Meanwhile, coke-like carbon was formed (C 1s at 284.2 eV).

To understand the difference between the role of nickel cations and that of metallic nickel atoms in adsorption of methane, we performed in-situ studies of $NiCo_2O_4$ in pure methane (no any oxygen gas) by AP-XPS. As shown in Supplementary Figures 10a and 10b, metallic Ni and Co are formed at a temperature higher than 300°C. Along the formation of metallic Ni, coke-like carbon is formed at a temperature higher than 300°C. This coke-like carbon couldn't be oxidized to CO_2 by introducing O_2 to the reactor at 400°C. Clearly, the C 1s of the carbon layer formed on $NiCo_2O_4$ in CH_4 (Supplementary Figure 10) is distinctly different from C 1s of the CH_n species formed on $NiCo_2O_4$ in the mixture of CH_4 and O_2 at 140°C (Supplementary Figure 8) and 400°C (Supplementary Figure 9).

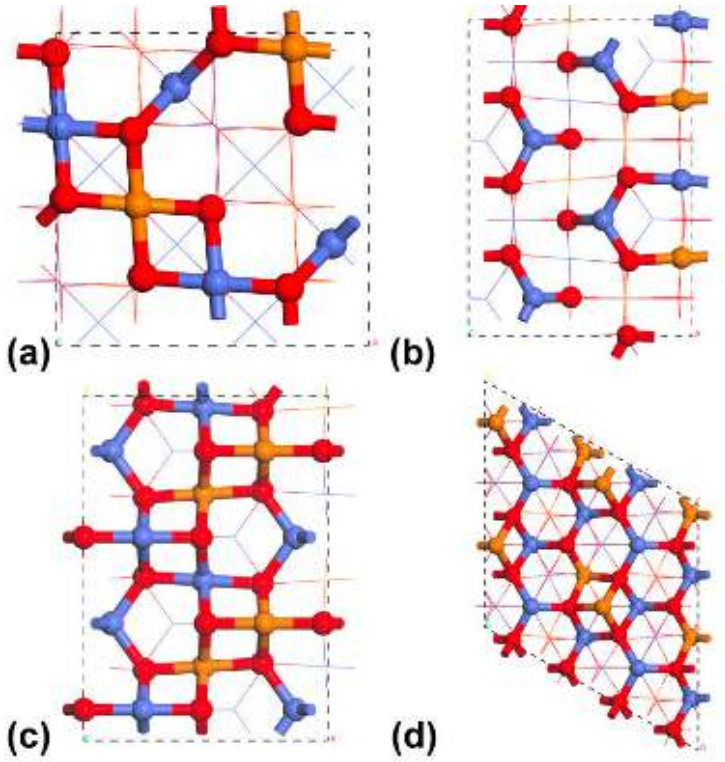

Supplementary Figure 11. Top views of the most commonly exposed surfaces of $NiCo_2O_4$ (crystal type I). (a) $NiCo_2O_4$(100), (b) $NiCo_2O_4$(110)-A, (c) $NiCo_2O_4$(110)-B, and (d) $NiCo_2O_4$(111). The carbon, hydrogen, oxygen, cobalt, and nickel atoms are shown in grey, white, red, blue, and yellow, respectively. The use of colors representing different atoms is implemented through the main text in the supporting information. The atoms on the top and sub-surfaces are illustrated in ball-and-stick model and the rest are in line model. This illustration is used throughout this report.

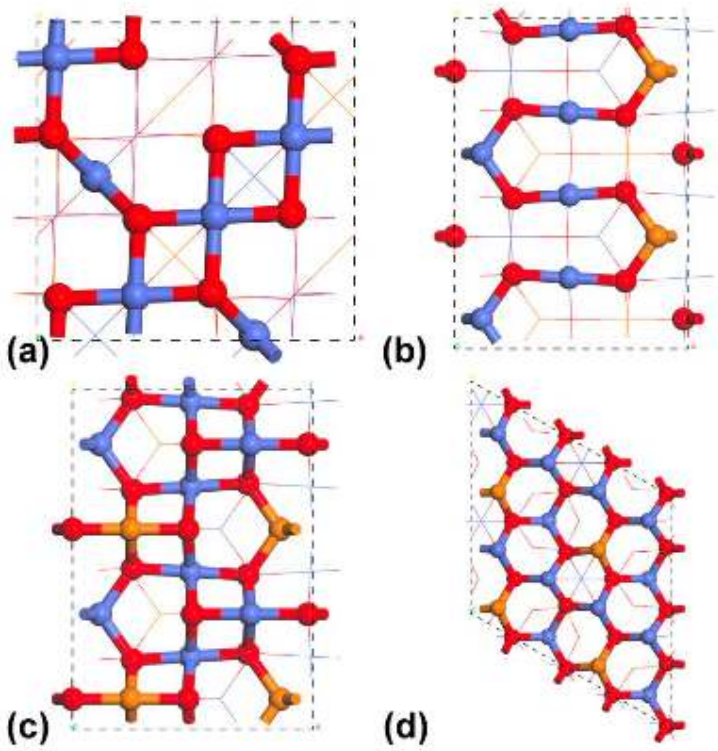

Supplementary Figure 12. Top views of the most commonly exposed surfaces of $NiCo_2O_4$ (crystal type II). (a) $NiCo_2O_4$(100), (b) $NiCo_2O_4$(110)-A, (c) $NiCo_2O_4$(110)-B, and (d) $NiCo_2O_4$(111).

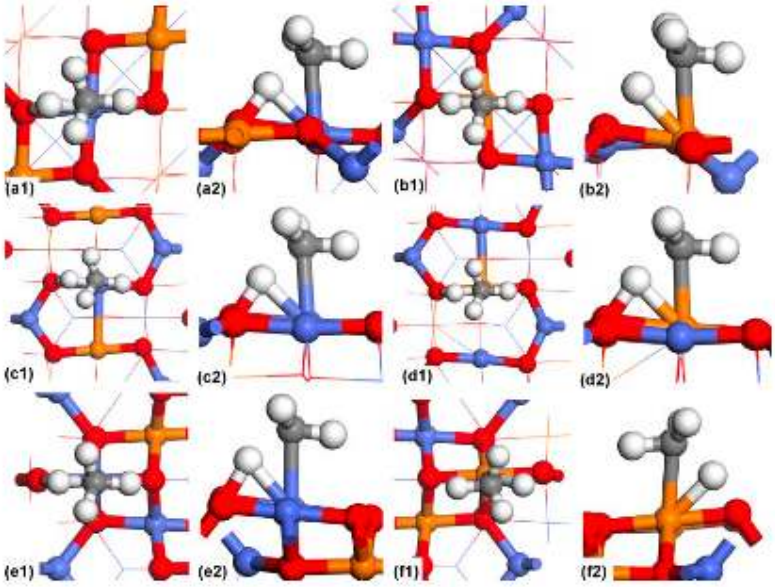

Supplementary Figure 13. Top and side views of geometries of transition states in the first C-H dissociation of CH_4 on Co or Ni cations of (100), (110-A), and (110-B) surface of type I crystal. *(a1) and (a2)*: top and side views of CH_4 on Co sites on (100), respectively. *(b1) and (b2)*: top and side views of CH_4 on Ni sites on (100), respectively. *(c1) and (c2)*: top and side views of CH_4 on Co sites on (110-A), respectively. *(d1) and (d2)*: top and side views of CH_4 on Ni sites on (110-A), respectively. *(e1) and (e2)*: top and side views of CH_4 on Co sites on (110-B), respectively. *(f1) and (f2):* top and side views of CH_4 on Ni sites on (110-B), respectively. The carbon, hydrogen, oxygen, cobalt, and nickel atoms are shown in grey, white, red, blue, and yellow, respectively. The use of colors representing different atoms is implemented through the main text in the supporting information. The activation barriers of these transition sates are listed in the second and third columns of Supplementary Table 2.

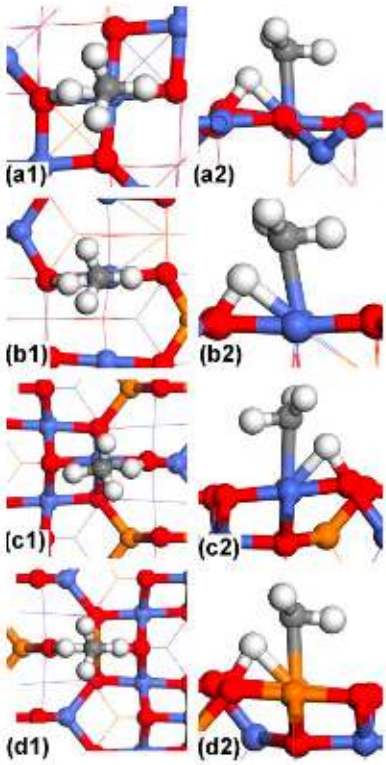

Supplementary Figure 14. Top and side views of geometries of transition state in the first C-H dissociation of CH_4 on Co or Ni cations of (100), (110-A), and (110-B) surfaces of type II crystal. *(a1) and (a2)*: top and side views of CH_4 on Co sites on (100), respectively. *(b1) and (b2)*: top and side views of CH_4 on Co sites on (100-A), respectively. *(c1) and (c2)*: top and side views of CH_4 on Co sites on (110-B), respectively. *(d1) and (d2)*: top and side views of CH_4 on Ni sites on (110-B), respectively. The activation barriers of these transition sates are listed in the fourth and fifth columns of Table 1 in the main text.

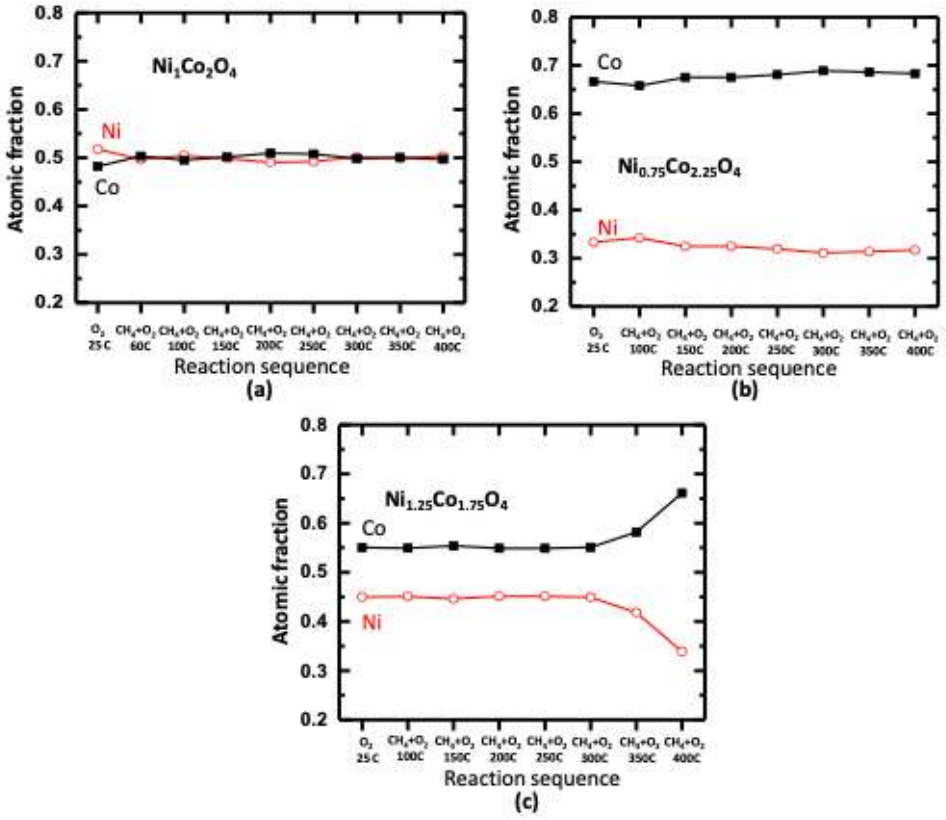

Supplementary Figure 15. Atomic fractions of Ni or Co cations in the total of Ni and Co cations on surface of $NiCo_2O_4$ (a), $Ni_{0.75}Co_{2.25}O_4$ (b), and $Ni_{1.25}Co_{1.75}O_4$ (c). The error of measurement of peak area is ±5% of the corresponding peak area. The atomic fractions of Ni cations were calculated with the following equation. As kinetic energies of photoelectrons from Ni 2p and Co 2p are very similar, they have similar mean free paths. Thus, the calculated atomic fraction of Ni or Co represents the fraction on the top-most surface under an assumption that Ni or Co are homogeneously distributed in surface layers.

$$Ni\% = \frac{\frac{A_{Ni2p}}{F_{Ni2p}}}{\frac{A_{Ni2p}}{F_{Ni2p}}+\frac{A_{Co2p}}{F_{Co2p}}} \times 100 \qquad (1)$$

$Ni_{0.75}Co_{2.25}O_4$ and $Ni_{1.25}Co_{1.75}O_4$ were synthesized with the same method as $NiCo_2O_4$. They are single phases of spinel oxide structure (Supplementary Figures 1b and 1c). The same measurements of catalytic performance show that they are active for combustion of CH_4 (Supplementary Figure 6). In-situ studies of $Ni_{0.75}Co_{2.25}O_4$ and $Ni_{1.25}Co_{1.75}O_4$ (Supplementary Figure 7) show that the atomic fractions of $\frac{Ni}{Ni+Co}$ of the surface layer of the three catalysts are different. For $NiCo_2O_4$, the atomic fractions of Ni and Co are 51% and 49% (Supplementary Figure 15a). They are 33% and 67% for Ni and Co on the surface of $Ni_{0.75}Co_{2.25}O_4$ (Supplementary Figure 15b) and 44% and 56% on $Ni_{1.25}Co_{1.75}O_4$ (Supplementary Figure 15c), respectively.

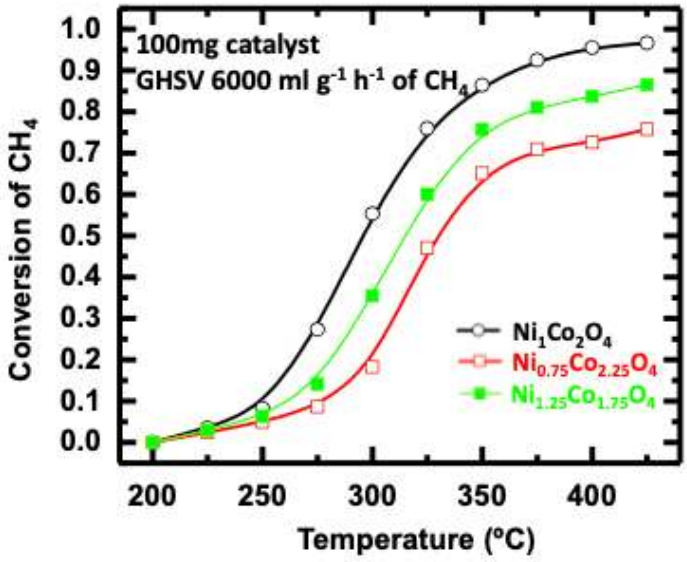

Supplementary Figure 16. Catalytic performances of $NiCo_2O_4$, $Ni_{1.25}Co_{1.75}O_4$ and $Ni_{0.75}Co_{2.25}O_4$ in the temperature range of 200-425°C at a GHSV of 6000 ml CH_4 g^{-1} h^{-1}. Although $Ni_{1.25}Co_{1.75}O_4$ and $Ni_{0.75}Co_{2.25}O_4$ are quite active for CH_4 combustion, they exhibit a lower conversion of CH_4 under the exactly same catalytic condition (GHSV of 6000 ml CH_4 $gram^{-1}$ h^{-1}) than $NiCo_2O_4$.

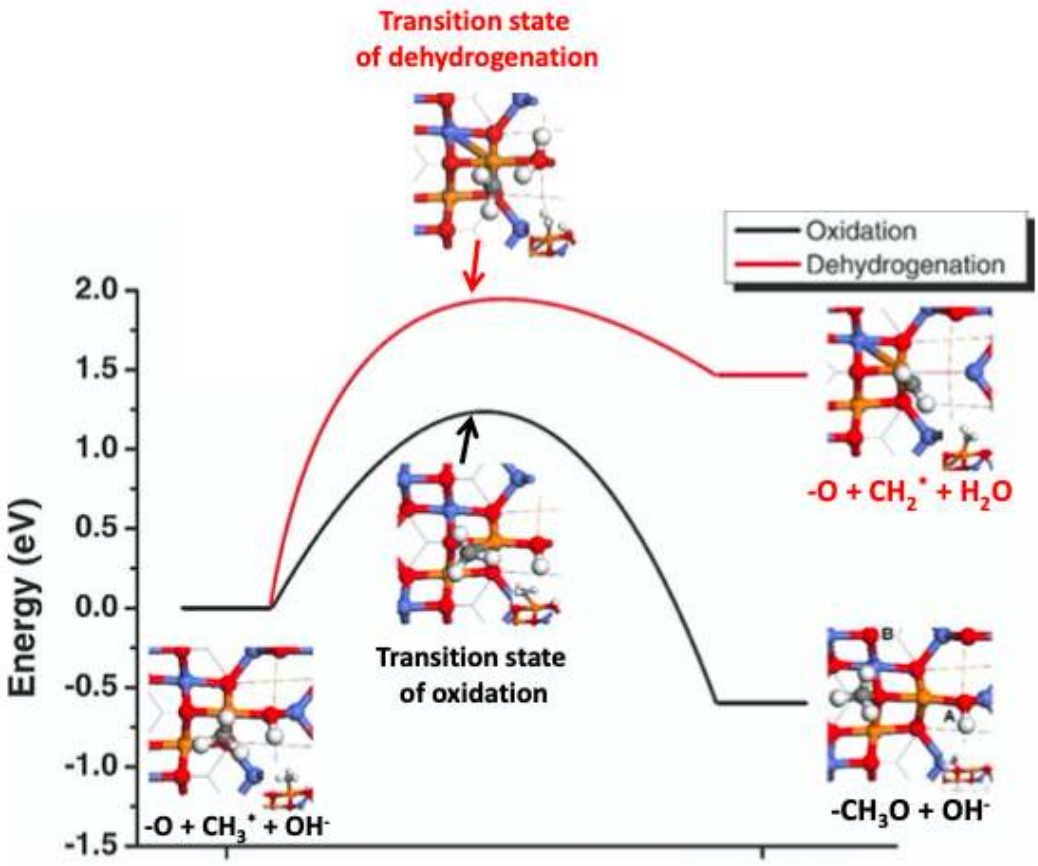

Supplementary Figure 17. Energy profiles of the pathway of CH_3 oxidation through coupling with surface lattice oxygen atom (black) and pathway of further dehydrogenation (red) on $NiCo_2O_4$(110-B). The geometry at the lower-left side shows the common initial state of [-O+CH_3*+OH-], while the final states of oxidation or dehydrogenation are illustrated at the lower right and upper right, respectively. The middle geometries are corresponding to the transition states of dehydrogenation and oxidation steps, respectively. The small inset at the lower-right corner of each of these structural modes is the side views of these structures. Nickel, cobalt and oxygen are shown in orange, blue and red, respectively. This notation is used throughout this paper.

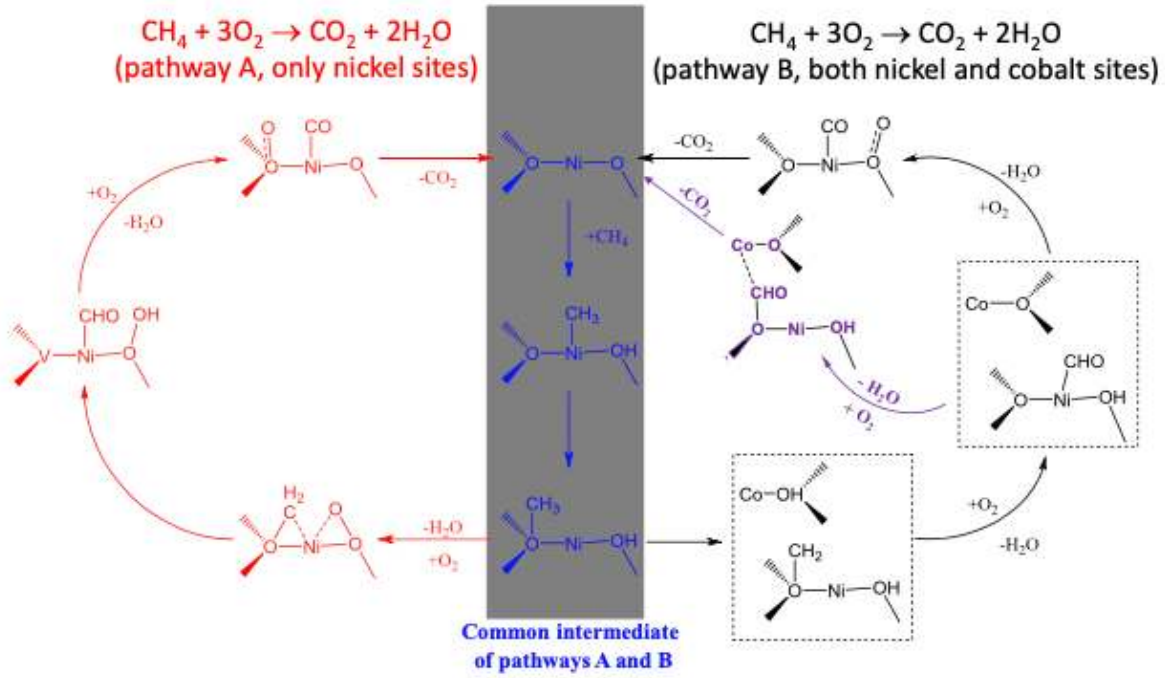

Supplementary Figure 18. Schematics of two different reaction pathways of methane complete oxidation on $NiCo_2O_4$(110-B) of type I crystal. The structures shown in blue on the middle of the schematic are the common intermediates for both pathways A and B; they are CH_3 formed through C-H dissociation and CH_3O formed through a coupling of carbon atom of CH_3 and oxygen atom of surface lattice. After CH_3O is formed, there are two different possible pathways A and B. Pathway A (shown in red) is the dehydrogenation by OH species of nickel site only, while pathway B (shown in black) is the dehydrogenation by oxygen species of nearby cobalt site .

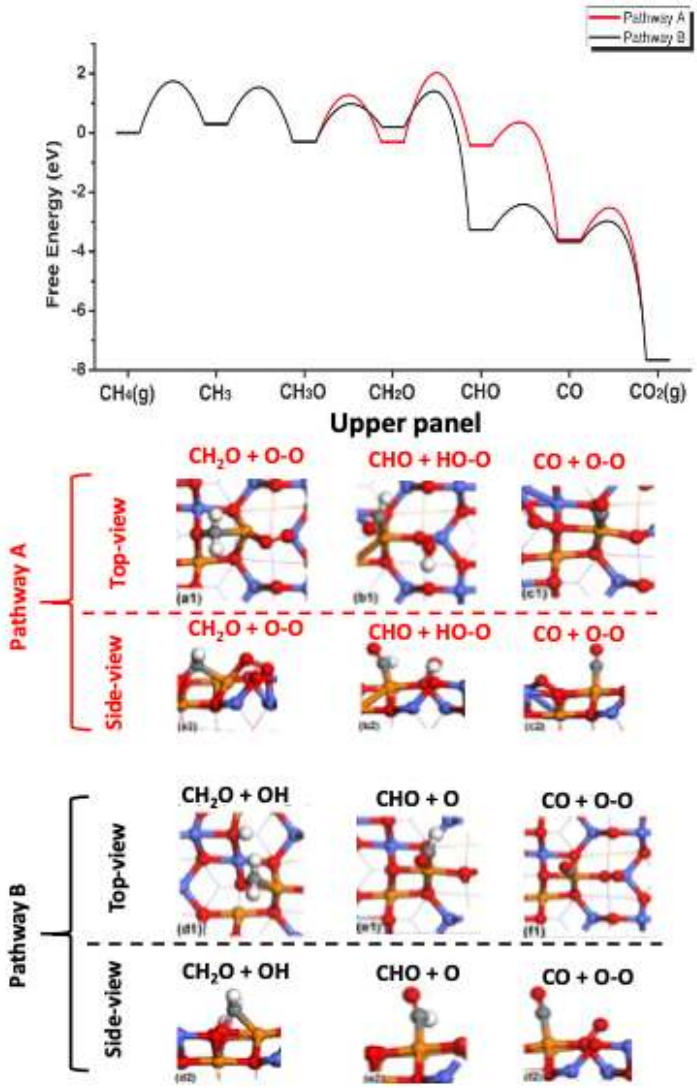

Supplementary Figure 19. The calculated energy profiles and optimized structures of intermediates along the pathway from reactants CH_4 and O_2 to products CO_2 and H_2O. Upper panel: Energy profile of pathways A (shown in red) and B (shown in black). The entropies of all the gas phase species are obtained at 823.15 K. **Middle panel:** Structures of intermediates of pathway A from reactants to products; Pathway A includes the CH_2O + O-O (a1 for top view and a2 for side view), CHO + HO-O (b1 for top view and b2 for side view), and CO + O-O (c1 for top view and c2 for side view). **Lower panel:** Structures of intermediates of pathway B from reactants to products; Pathway B includes CH_2O + OH (d1 for top view and d2 for side view), CHO + O (e1 for top view and e2 for side view), and CO + O-O (f1 for top view and f2 for side view). It is noted that the elementary steps for transformation of intermediate CHO to products CO_2 and H_2O presented here is the sub-pathway of CO oxidation. Other than the sub-pathway of CO oxidation for the transformation of intermediate CHO to products presented in this figure, an alternative one is called sub-pathway of OCHO dehydrogenation which is presented in Supplementary Figure 21.

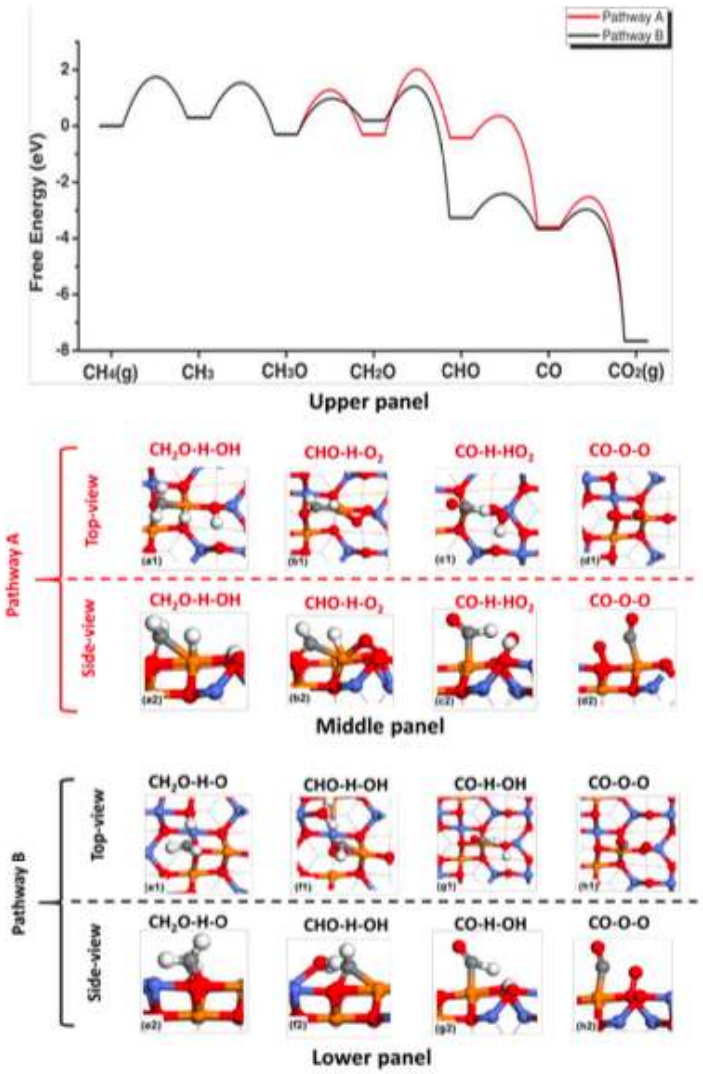

Supplementary Figure 20. The calculated energy profiles and optimized structures of transition states along the pathways A and B from reactants CH_4 and O_2 to products CO_2 and H_2O. Upper panel: Energy profile of pathways A (shown in red) and B (shown in black). **Middle panel:** Structures of transition states of pathway A from reactants to products; pathway A includes transition states CH_2O-H-OH (a1 for top view and a2 for side view), CHO-H-O_2 (b1 for top view and b2 for side view), CO-H-HO_2 (c1 for top view and c2 for side view), and CO-O-O (d1 for top view and d2 for side view). **Lower panel:** Structures of transition states of pathway B from reactants to products; pathway B includes CH_2O-H-O (e1 for top view and e2 for side view), CHO-H-OH (f1 for top view and f2 for side view), CO-H-OH (g1 for top view and g2 for side view), and CO-O-O (h1 for top view and h2 for side view). It is noted that the elementary steps for transformation of intermediate CHO to products CO_2 and H_2O in pathway B are called *sub-pathway of CO oxidation*. Other than the shown sub-pathway of CO oxidation for the transformation of intermediate CHO to products, alternative elementary steps are called *sub-pathway of OCHO dehydrogenation*. The calculated energy profiles of the two sub-pathway are given in Figures 14a and 14b of the main text. The structures of transition states and intermediates of the two parallel sub-pathways of pathway B are presented in Figures 14c and 14d, respectively. They are discussed in the main text in detailed. A comparison between the sub-pathway of CO oxidation and the sub-pathway of OCHO dehydrogenation are given in the main text as well.

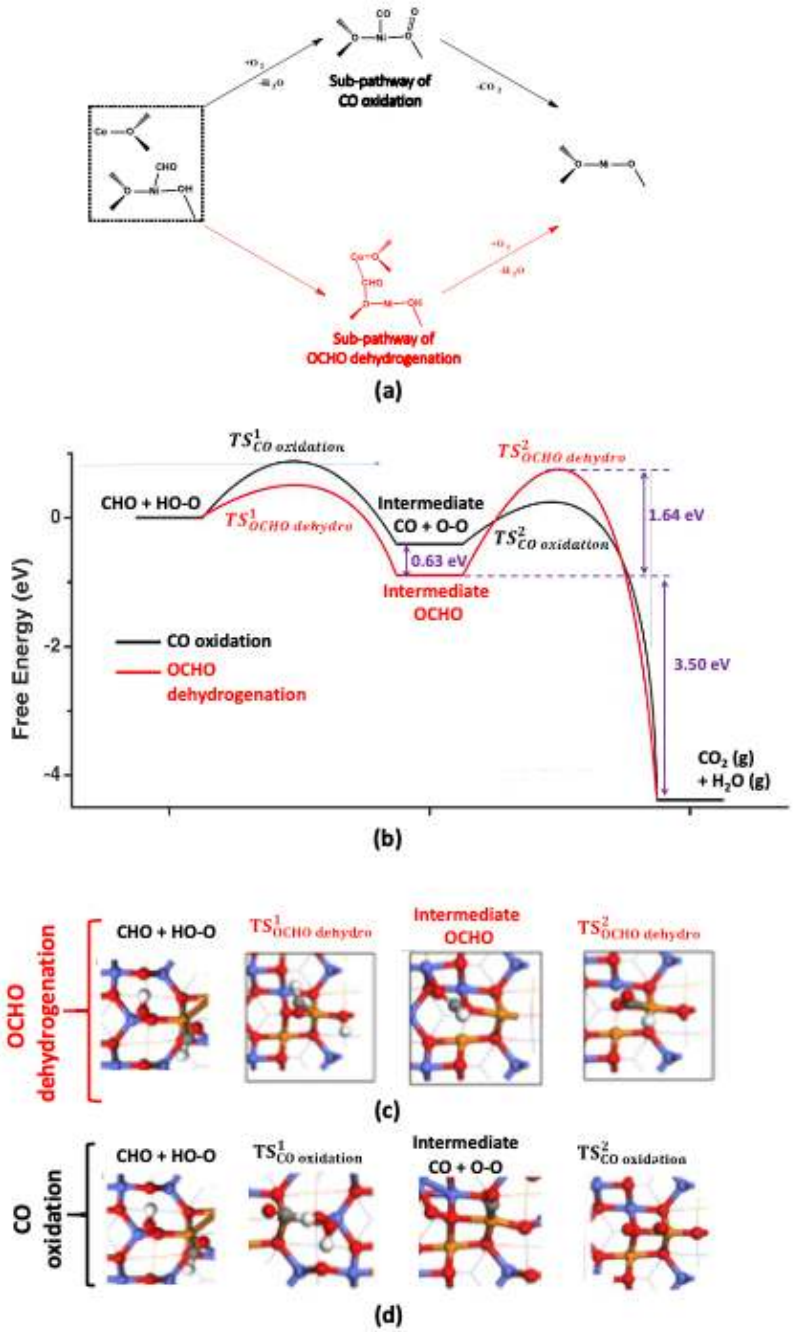

Supplementary Figure 21. DFT calculations of sub-pathways for transforming CHO to product molecules. Each sub-pathway includes two elemental steps with two transition states and one intermediate. (a) Two different sub-pathways for the transformation of CHO to products, including the sub-pathway of CO oxidation (shown in black) which is the last part of pathway B in Figure 12 and the sub-pathway of OCHO dehydrogenation (shown in red). **(b)** Calculated energy profiles and optimized intermediates (CO+O-O versus OCHO) and transition states for the transformation of CHO to product CO_2 on $NiCo_2O_4$(110-B) of type I crystal after

CHO is formed in pathway B. The elemental steps involved in this transformation (from CHO to products) are called a sub-pathway. For this transformation, the sub-pathway of CO oxidation is the last part of pathway B in Figure 12. Other than this sub-pathway, sub-pathway of OCHO dehydrogenation (red line) was proposed and calculated. **(c)** Optimized structures of transition states and intermediate of the sub-pathway of OCHO dehydrogenation. **(d)** Optimized structure of transition states and intermediate of the sub-pathway of CO oxidation.

Supplementary Table 1. The surface energies of four different surfaces, namely 100, 110-A, 110-B and 111, of type I and type II crystals. All the surface energies are in $eV/Å^2$. It is noted that the difference in energy of 0.01 eV could make a big difference in surface energy; for example, the difference of Cu(111) and Cu(100) is less than 0.01 eV.

	Type I	Type II
100	0.07	0.07
110-A	0.09	0.10
110-B	0.09	0.10
111	0.17	0.14

Supplementary Table 2. The activation barriers of the first C-H of CH_4 on three different facets (100, 110-A and 110-B) of crystal types I and II. In addition, our calculations show that the activation barriers on the surface of pure Co_3O_4 (110-B) are 0.38 eV higher than the $NiCo_2O_{4-x}$ (110-B) of type I crystal, which suggests that doping nickel cations in Co_3O_4 could significantly enhance the reactivity by decreasing the activation barrier of the first C-H of CH_4.

Crystal type	Type I		Type II	
Site for the dissociation of the first C-H of CH_4	Co^{3+}	Ni^{3+}	Co^{3+}	Ni^{3+}
100 surface	0.91	1.22	0.83	N/A
110-A surface	1.06	1.12	0.65	N/A
110-B surface	0.90	0.52	0.80	0.73

Supplementary Methods

Calculation of surface area of $NiCo_2O_4$ nanoparticles with average size of 4.5 nm

$NiCo_2O_4$ has the same lattice as Co_3O_4 in terms of structure of spinel oxide. As the lattice constant of $NiCo_2O_4$ is very close to Co_3O_4 and the molecular mass of $NiCo_2O_4$ is very close to Co_3O_4, surface area of 1 gram of $NiCo_2O_4$ with an average size of 4.5 nm is very similar to 1 gram of Co_3O_4 with an average size of 4.5 nm. To simplify the evaluation of the surface area, the surface area of 1 gram of $NiCo_2O_4$ nanocube with an average size of 4.5 nm can be calculated as the following.

(1) The number of nanocubes in 1 g of Co_3O_4:

$$N_{Co_3O_4} = \frac{V_{1\ gram\ of\ Co_3O_4}}{V_{a\ Co_3O_4\ nanocube}} = \frac{1\ g/\rho_{Co_3O_4}}{V_{a\ Co_3O_4\ nanocube}} \qquad (2)$$

Here $\rho_{Co_3O_4}$ is the density of Co_3O_4, $V_{a\ Co_3O_4 nanocube}$ is the volume of a Co_3O_4 nanocube. If we assume that the shape of the nanoparticle is cubic with the average size of 4.5 nm, $V_{a\ Co_3O_4\ nanocube}$ equals $4.5^3\ nm^3 = 91.125\ nm^3$.

As $\rho_{Co_3O_4}\ is\ 6.11\ g/cm^3 or\ 6.11 \times 10^{-21}\ g/nm^3$,

$$N_{Co_3O_4} = \frac{V_{Co_3O_4}}{V_{a\ Co_3O_4 nanocube}} = \frac{1\ g/\rho_{Co_3O_4}}{V_{a\ Co_3O_4\ naniocube}} = \frac{1\ g/6.11 \times 10^{-21}\ g/nm^3}{91.125\ nm^3} = 1.80 \times 10^{18}$$

(2) Surface area of one Co_3O_4 nanocube: $S_{a\ Co_3O_4\ nanocube}$

$6 \times 4.5^2\ nm^2 = 121.5\ nm^2$,

(3) Surface area of 1 g of Co_3O_4 in which the average size of Co_3O_4 nanocubes is 4.5 nm

$$S_{Co_3O_4} = N_{Co_3O_4} \times S_{a\ Co_3O_4\ nanocube} = 1.80 \times 10^{18} \times 121.5\ nm^2 \qquad (3)$$

$$= 2.187 \times 10^{20}\ nm^2 = 218.7\ m^2$$